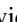



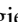


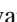








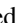


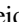





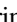




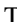
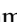

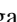


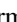






PHANGS–JWST First Results: The Dust Filament Network of NGC 628 and Its Relation to Star Formation Activity

David A. Thilker¹ , Janice C. Lee² , Sinan Deger^{3,4} , Ashley T. Barnes⁵ , Frank Bigiel⁵ , Médéric Boquien⁶ , Yixian Cao⁷ , Mélanie Chevance^{8,9} , Daniel A. Dale¹⁰ , Oleg V. Egorov^{8,11} , Simon C. O. Glover¹² , Kathryn Grasha¹³ , Jonathan D. Henshaw^{14,15} , Ralf S. Klessen^{12,16} , Eric Koch¹⁷ , J. M. Diederik Kruijssen⁹ , Adam K. Leroy¹⁸ , Ryan A. Lessing¹ , Sharon E. Meidt¹⁹ , Francesca Pinna¹⁵ , Miguel Querejeta²⁰ , Erik Rosolowsky²¹ , Karin M. Sandstrom²² , Eva Schinnerer¹⁵ , Rowan J. Smith²³ , Elizabeth J. Watkins⁸ , Thomas G. Williams¹⁵ , Gagandeep S. Anand²⁴ , Francesco Belfiore²⁵ , Guillermo A. Blanc^{26,27} , Rupali Chandar²⁸ , Enrico Congiui²⁷ , Eric Emsellem^{29,30} , Brent Groves^{13,31} , Kathryn Kreckel⁸ , Kirsten L. Larson³² , Daizhong Liu³³ , Ismael Pessa^{15,34} , and Bradley C. Whitmore²⁴ 

¹ Department of Physics and Astronomy, The Johns Hopkins University, Baltimore, MD 21218, USA; dthilker@jhu.edu

² Gemini Observatory/NSF's NOIRLab, 950 N. Cherry Avenue, Tucson, AZ, 85719, USA

³ California Institute of Technology, 1200 E. California Boulevard., MC 249-17, Pasadena, CA 91125, USA

⁴ The Oskar Klein Centre for Cosmoparticle Physics, Department of Physics, Stockholm University, AlbaNova, Stockholm, SE-106 91, Sweden

⁵ Argelander-Institut für Astronomie, Universität Bonn, Auf dem Hügel 71, D-53121 Bonn, Germany

⁶ Centro de Astronomía (CITEVA), Universidad de Antofagasta, Avenida Angamos 601, Antofagasta, Chile

⁷ Max-Planck-Institut für Extraterrestrische Physik (MPE), Giessenbachstr. 1, D-85748 Garching, Germany

⁸ Astronomisches Rechen-Institut, Zentrum für Astronomie der Universität Heidelberg, Mönchhofstraße 12-14, D-69120 Heidelberg, Germany

⁹ Cosmic Origins of Life (COOL) Research DAO³⁵

¹⁰ Department of Physics and Astronomy, University of Wyoming, Laramie, WY 82071, USA

¹¹ Sternberg Astronomical Institute, Lomonosov Moscow State University, Universitetsky pr. 13, 119234 Moscow, Russia

¹² Universität Heidelberg, Zentrum für Astronomie, Institut für Theoretische Astrophysik, Albert-Ueberle-Str 2, D-69120 Heidelberg, Germany

¹³ Research School of Astronomy and Astrophysics, Australian National University, Canberra, ACT 2611, Australia

¹⁴ Astrophysics Research Institute, Liverpool John Moores University, 146 Brownlow Hill, Liverpool L3 5RF, UK

¹⁵ Max-Planck-Institut für Astronomie, Königstuhl 17, D-69117 Heidelberg, Germany

¹⁶ Universität Heidelberg, Interdisziplinäres Zentrum für Wissenschaftliches Rechnen, Im Neuenheimer Feld 205, D-69120 Heidelberg, Germany

¹⁷ Harvard-Smithsonian Center for Astrophysics, 60 Garden Street, Cambridge, MA 02138, USA

¹⁸ Department of Astronomy, The Ohio State University, 140 West 18th Avenue, Columbus, Ohio 43210, USA

¹⁹ Sterrenkundig Observatorium, Universiteit Gent, Krijgslaan 281 S9, B-9000 Gent, Belgium

²⁰ Observatorio Astronómico Nacional (IGN), C/Alfonso XII, 3, E-28014 Madrid, Spain

²¹ Department of Physics, University of Alberta, Edmonton, AB T6G 2E1, Canada

²² Center for Astrophysics and Space Sciences, Department of Physics, University of California, San Diego, 9500 Gilman Drive, La Jolla, CA 92093, USA

²³ Jodrell Bank Center for Astrophysics, Department of Physics and Astronomy, University of Manchester, Oxford Road, Manchester M13 9PL, UK

²⁴ Space Telescope Science Institute, 3700 San Martin Drive, Baltimore, MD 21218, USA

²⁵ INAF—Osservatorio Astrofisico di Arcetri, Largo E. Fermi 5, I-50157, Firenze, Italy

²⁶ Observatories of the Carnegie Institution for Science, 813 Santa Barbara Street, Pasadena, CA 91101, USA

²⁷ Departamento de Astronomía, Universidad de Chile, Camino del Observatorio 1515, Las Condes, Santiago, Chile

²⁸ University of Toledo, 2801 W. Bancroft Street, Mail Stop 111, Toledo, OH, 43606, USA

²⁹ European Southern Observatory, Karl-Schwarzschild Straße 2, D-85748 Garching bei München, Germany

³⁰ Univ Lyon, Univ Lyon 1, ENS de Lyon, CNRS, Centre de Recherche Astrophysique de Lyon UMR5574, F-69230 Saint-Genis-Laval, France

³¹ International Centre for Radio Astronomy Research, University of Western Australia, 35 Stirling Highway, Crawley, WA 6009, Australia

³² AURA for the European Space Agency (ESA), Space Telescope Science Institute, 3700 San Martin Drive, Baltimore, MD 21218, USA

³³ Max-Planck-Institut für extraterrestrische Physik, Giessenbachstraße 1, D-85748 Garching, Germany

³⁴ Leibniz-Institut für Astrophysik Potsdam (AIP), An der Sternwarte 16, 14482 Potsdam, Germany

Received 2022 October 27; revised 2022 December 15; accepted 2022 December 22; published 2023 February 16

Abstract

PHANGS–JWST mid-infrared (MIR) imaging of nearby spiral galaxies has revealed ubiquitous filaments of dust emission in intricate detail. We present a pilot study to systematically map the dust filament network (DFN) at multiple scales between 25 and 400 pc in NGC 628. MIRI images at 7.7, 10, 11.3, and 21 μm of NGC 628 are used to generate maps of the filaments in emission, while PHANGS–HST *B*-band imaging yields maps of dust attenuation features. We quantify the correspondence between filaments traced by MIR thermal continuum/polycyclic aromatic hydrocarbon (PAH) emission and filaments detected via extinction/scattering of visible light; the fraction of MIR flux contained in the DFN; and the fraction of H II regions, young star clusters, and associations within the DFN. We examine the dependence of these quantities on the physical scale at which the DFN is extracted. With our highest-resolution DFN maps (25 pc filament width), we find that filaments in emission and attenuation are cospatial in 40% of sight lines, often exhibiting detailed morphological agreement; that $\sim 30\%$

of the MIR flux is associated with the DFN; and that 75%–80% of the star formation in H II regions and 60% of the mass in star clusters younger than 5 Myr are contained within the DFN. However, the DFN at this scale is anticorrelated with looser associations of stars younger than 5 Myr identified using PHANGS–HST near-UV imaging. We discuss the impact of these findings on studies of star formation and the interstellar medium, and the broad range of new investigations enabled by multiscale maps of the DFN.

Unified Astronomy Thesaurus concepts: [Interstellar medium \(847\)](#); [Interstellar filaments \(842\)](#); [Interstellar dust \(836\)](#); [Dust continuum emission \(412\)](#); [Extinction \(505\)](#); [Star formation \(1569\)](#); [Star forming regions \(1565\)](#)

Supporting material: figure set

1. Introduction

Two overwhelming impressions from inspecting JWST images of nearby galaxies are the sheer number of resolved stars seen in the near-IR (NIR) and the stunning degree of structured, filamentary mid-IR (MIR) emission originating from small dust grains and polycyclic aromatic hydrocarbons (PAHs) in the interstellar medium (ISM). JWST provides the spatial resolution necessary to cleanly decompose the observed MIR dust emission into filament features, discrete compact sources, and a diffuse component throughout the Local Volume ($d \lesssim 11$ Mpc) and beyond, as could only previously be done in the Local Group (Hinze et al. 2004; Barmby et al. 2006; Verley et al. 2007, 2009). This is of astrophysical importance not only because dust plays a central role in enabling star formation but also hides the youngest clusters and star-forming regions from view at short wavelengths. In HST, optical multicolor imaging of star-forming galaxies, dust lanes stand out as highly structured attenuation features (La Vigne et al. 2006; Dong et al. 2016) occasionally punctuated by H II regions and clusters that have pierced the veil of their dusty natal molecular cloud.

The observation of such abundant organized extragalactic structure in dust emission and attenuation is tantalizing because studies of the cold gas and dust in the Milky Way have revealed filaments (Jackson et al. 2010) of length >100 pc that have even been dubbed the “bones” of the Milky Way’s cold ISM (Goodman et al. 2014; Ragan et al. 2014; Zucker et al. 2015; Soler et al. 2020). Indeed, much recent work in the Milky Way points toward a view of the cold, dusty star-forming medium that is filamentary and multiscale (Zucker et al. 2018; Hacar et al. 2022; Pineda et al. 2022), very different from the classical “spherical molecular cloud.” The filamentary structure even persists at subparsec, cloud-substructure scales (e.g., André et al. 2010; André et al. 2014), though in the Local Volume extragalactic context, we are limited to studying larger filaments (akin to those of Syed et al. 2022). The shift to a filament-centered paradigm implies that criteria for stability and fragmentation change, becoming a mass per unit length threshold rather than a more traditional Jeans mass argument. All this filamentary structure seeds star formation and determines the rate and efficiency of collapse and defines the medium that the stellar feedback is subsequently driven into, thereby determining how feedback drives the baryon cycle within galaxies.

A revolution in our view of the dust structure in nearby galaxies is underway, having overcome the barrier of resolution with the combined capabilities of JWST and HST. This enhanced extragalactic perspective is a critical advance because we only have observations of the Milky Way from within, making them subject to distance uncertainties and line-of-sight projection ambiguities. Milky Way–based studies of dust filament structures do sample substantially smaller physical

scales than even JWST can reach in nearby galaxies, and the use of distance-tagged Gaia measurements to infer 3D extinction maps (e.g., Sale & Magorrian 2018; Green et al. 2019; Lallement et al. 2019; Leike & Enßlin 2019), combined with a focus on dust emission out of the plane, together helps mitigate confusion. Indeed, recent studies comparing the 3D filament structures in extinction with 2D emission maps have shown a remarkable correspondence between dust tracers (e.g., Bialy et al. 2021; Hottier et al. 2021; Zucker et al. 2021; Dharmawardena et al. 2022, 2023). Nevertheless, we emphasize that the area of the Milky Way disk probed by these techniques is quite limited ($d \leq 3$ kpc). In external galaxies, we can now quantify entire dust filament networks (DFNs)³⁶ on scales ranging from the size of individual GMCs up to morphological features dominating entire galaxies and reveal their intimate connection with respect to star formation, feedback, and dynamical mechanisms. This new era of dusty ISM cartography will leverage representative galaxy samples to provide systematic answers to how the prevalence and properties of these filamentary features may depend on the galactic environment; whether they universally form the backbone of the cold ISM, through comparison to CO maps; and how the joint dust and molecular gas distribution is related to structures like spiral arms and bars, contrasted to high-resolution parsec-scale UV+IR tracers of star formation activity from HST and JWST. Critically, the new observations can be directly compared to state-of-the-art galaxy simulations (e.g., Smith et al. 2014a; Duarte-Cabral et al. 2015; Duarte-Cabral & Dobbs 2017; Jeffreson et al. 2020; Smith et al. 2020; Tress et al. 2020; Treß et al. 2021).

JWST resolution and depth are sufficient to recover filamentary dust emission features, at GMC scales, analogous to those of the Milky Way in galaxies out to roughly the distance of the Virgo cluster. This Letter focuses on NGC 628 (also known as Messier 74, “The Phantom Galaxy”), an archetypal face-on SA(s)c galaxy (Buta et al. 2015). NGC 628 is nearby ($d = 9.84 \pm 0.03$ Mpc; Anand et al. 2021a, 2021b), star-forming ($\text{SFR} = 1.8 \pm 0.45 M_{\odot} \text{yr}^{-1}$), massive ($M_{*} = 2.2 \pm 0.56 \times 10^{10} M_{\odot}$), and viewed at a low inclination ($i \sim 9^{\circ} \pm 12^{\circ}$, Lang et al. 2020). NGC 628 is part of a broader sample of 19 “main-sequence” star-forming galaxies for which systematic, uniform surveys with HST (Lee et al. 2022), ALMA (Leroy et al. 2021), VLT-MUSE (Emsellem et al. 2022), and now JWST (Lee et al. 2023, this

³⁶ All of the first four PHANGS–JWST galaxies observed show prominent structuring of the disk into a DFN. For this reason, we coin the acronym DFN with confidence that it will be frequently used. The concept of a filament network is not new (e.g., Smith et al. 2014b; André et al. 2014; Smith et al. 2016; Hacar et al. 2022), but MIRI has revealed such complex multiscale structuring is commonplace.

Issue) have been carried out by the PHANGS (Physics at High Angular resolution in Nearby GalaxieS) collaboration.³⁷

2. Data

2.1. PHANGS–JWST Imaging

NGC 628 is one of the initial targets observed for the PHANGS–JWST Cycle 1 Treasury project (GO 2107, PI J. Lee). Our observations of NGC 628 target the central region ($R_{\text{gal}} \lesssim 5$ kpc) of the star-forming disk to overlap areas where HST, ALMA, and MUSE data have been obtained.³⁸ The data set includes imaging with NIRCcam (F200W, F300M, F335M, and F360M) and MIRI (F770W, F1000W, F1130W, and F2100W). Photospheric emission from resolved stellar populations is a major component in the four NIRCcam bands (excepting F335M, which primarily probes the $3.3 \mu\text{m}$ PAH feature), whereas MIRI traces the ISM (both PAHs and hot, small dust grains). The resolution varies from $0''.066$ to $0''.12$ (NIRCcam) and $0''.25$ to $0''.67$ (MIRI). For MIRI, this corresponds to 12–32 pc at the distance of NGC 628. A detailed description of the PHANGS–JWST observations and data reduction is presented by Lee et al. (2023, this Issue).³⁹ Here, we focus on MIRI imaging, deferring analysis of filamentary structure seen in the $3.3 \mu\text{m}$ PAH feature to future work in anticipation of improved astrometric alignment among the PHANGS–JWST NIRCcam and MIRI imaging. Of particular importance to the analysis in Section 4.2 is the sky background adopted for the MIRI data. We use background-corrected images that have been tied to the sky level measured in wide-field Spitzer and WISE archival imaging, as described in the Appendix of Leroy et al. (2023, this Issue). The MIRI background levels are currently uncertain by ± 0.1 MJy sr^{-1} .

2.2. PHANGS–HST Imaging

The HST NUV–*U*–*B*–*V*–*I* (F275W, F336W, F435W, F555W, F814W) observations of the central NGC 628 disk we use were obtained by LEGUS (GO 13364, Calzetti et al. 2015) using WFC3/UVIS for NUV and *U*, and by R. Chandar (GO 10402) using ACS/WFC for *B*, *V*, and *I*. All data were reprocessed by PHANGS–HST. Full details are given in Lee et al. (2022). The ACS/WFC *B*-band images we use to identify dust lanes in attenuation have a resolution ($\sim 0''.09$, 4.3 pc), approximately $2.5\times$ finer than MIRI F770W.

2.3. MUSE H II Region Catalog

We use the nebular catalog of H II regions derived from the integral field unit (IFU) spectroscopy of the PHANGS–MUSE survey Emsellem et al. (2022). For NGC 628, the “convolved, optimized” resolution in PHANGS–MUSE DR 2.2 is $0''.92$, corresponding to a spatial resolution of 44 pc. Santoro et al. (2022) and Groves et al. (2022) used PHANGS–MUSE data to create a catalog of H II regions and provide fluxes corrected for Milky Way and internal extinction. Only star-forming regions

classified using the BPT diagram (Baldwin et al. 1981) are retained in our analysis.

2.4. HST Stellar Association and Cluster Catalogs

PHANGS–HST-resolved stellar photometry has been used to identify and characterize stellar associations as summarized in (Lee et al. 2022) and described in detail by Larson et al. (2022). Stellar clusters in NGC 628 have been studied by Thilker et al. (2022). PHANGS–HST catalogs are publicly available.⁴⁰ For both associations and clusters, fluxes for the five available HST bands were measured (using upper limits in nondetected photometric bands) and then age, mass, and reddening were estimated⁴¹ via fitting of observed SEDs (Turner et al. 2021) to solar-metallicity stellar population models using CIGALE (Boquien et al. 2019).

We use the PHANGS–HST associations catalog based on local overdensities of NUV point-like detections at a scale of 32 pc for our analysis. The stellar associations have ages ranging up to $\sim 10^2$ Myr. We use a subset selected to have age less than 5 Myr in order to limit the population to the most recent star formation activity. Clusters for our analysis were also selected with the same upper limit on age.

3. Dust Filament Analysis

3.1. Filament Extraction

We identify dust filaments using FILFINDER (Koch & Rosolowsky 2015). This code applies an adaptive thresholding algorithm and graph-based medial skeleton analysis to isolate and then characterize filaments. Thresholding is conducted over local neighborhoods, allowing for the extraction of structure over a large dynamic range both in intensity and spatial scale (the latter when the code is run multiple times with different parameter choices). The potential effect of bright sources interspersed in the web of filaments is mitigated by an arctan intensity transform before thresholding. We use a slightly modified version of FILFINDER in which the arctan-transformed image is convolved to the filament extraction scale before each run. In the current analysis we only utilize the filament masks produced by the code, leaving FILFINDER’s skeleton analysis capabilities for future work.

We apply FILFINDER independently to the background-corrected image in each MIRI band and to a preprocessed version of the *B*-band HST image (in which attenuation features are most evident compared to NUV, *U*, *V*, and *I*).

For preprocessing the HST image, multiscale median filtering is used to suppress peak-like features over a range in scale, while retaining small-scale dips (concave areas). Our specific filtering method follows from Hoversten et al. (2011). At each pixel, the output value is assigned to be that location’s minimum in a stack of circular median-filtered images. Filter kernel diameters are taken from a ladder of physical scales (starting at the resolution limit and proceeding up to 32 pc). The result is that confusion by bright stars and stellar clusters is greatly reduced, emphasizing the dust lane structures. Figure 1 (left) and Figure 6 (left) show the preprocessed image. FILFINDER nominally operates by finding positive filamentary features above the background. Therefore, before passing the

³⁷ <https://sites.google.com/view/phangs/home>

³⁸ Footprint maps of the HST, ALMA, and MUSE observations are available at <https://archive.stsci.edu/hlsp/phangs-hst> (10.17909/t9-r08f-dq31). Science-ready PHANGS–HST images are also available for download.

³⁹ Preliminary JWST image products are available at the Canadian Astronomy Data Centre CANFAR PHANGS–JWST Treasury Survey Data publication:10.11570/22.0082

⁴⁰ On MAST at <https://archive.stsci.edu/hlsp/phangs-cat> (10.17909/jray-9798)

⁴¹ Degeneracy between age and reddening is apparent for a subset of objects and could be more relevant in our dust filaments.

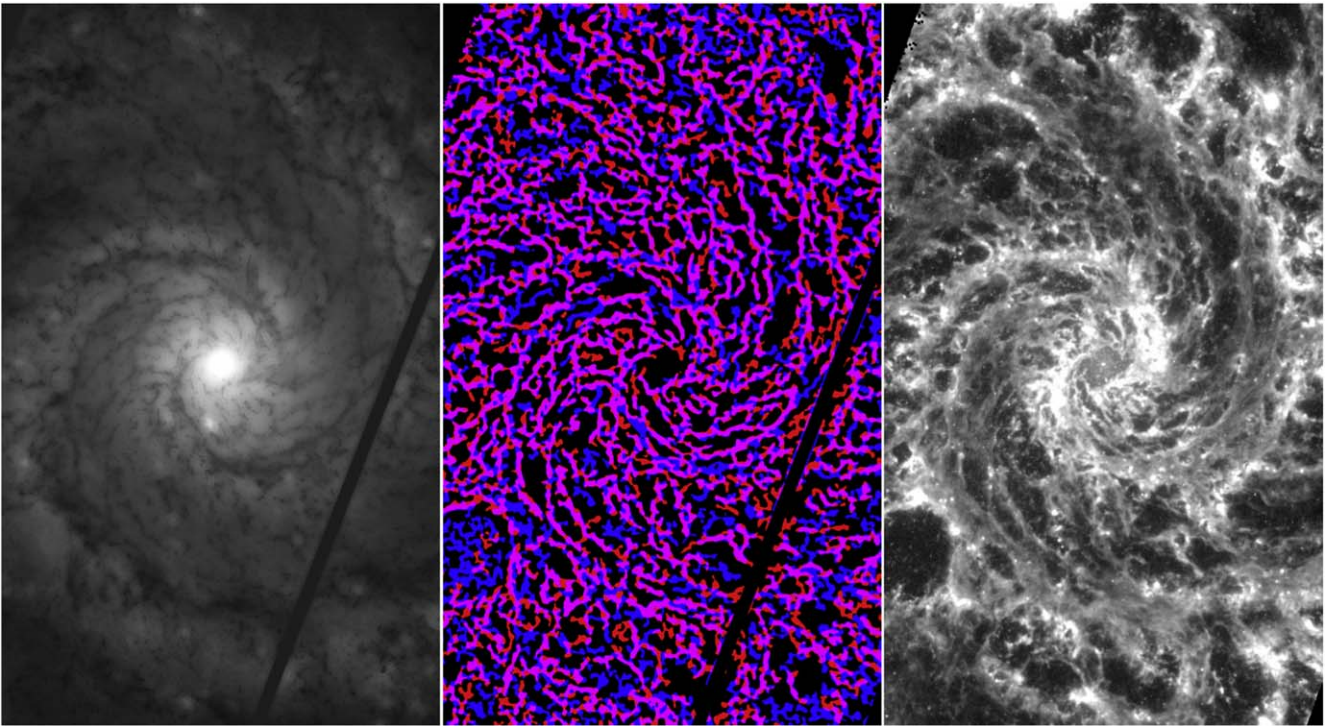


Figure 1. A first comparison of dust filaments identified in absorption and emission. Left: preprocessed B -band HST image, filtered to remove compact positive sources but retain small negative/concave morphological features. Center: filament masks for visible attenuation (blue) and MIR emission (red) extracted at a scale of 25 pc. Areas of overlap appear magenta. Right: JWST/MIRI F770W image. North is up, east is left, and the field of view spans 7.3 kpc from top to bottom. The figure only shows a portion of the area observed with JWST. The entire image may be seen in Figures 5 and A1–A4.

preprocessed B -band image to FILFINDER, we invert the sense of the intensity (subtracting the image from a constant value equal to the maximum in the field of view), so that dust attenuation filaments appear as the positive features expected by FILFINDER.

For both attenuation and emission, we use FILFINDER to identify potential filaments with narrow dimension (width) starting at 25 pc then stepping by factors of UNDEFINED (0.15 dex) up to 400 pc (25, 35, 50, 70, 100, 140, 200, 280, 400 pc). The minimum scale of 25 pc corresponds to approximately twice the PSF FWHM of MIRI F770W. For F2100W analysis, we begin at the 35 pc scale due to the larger F2100W PSF. FILFINDER parameters are set as follows: $\text{size_thresh} = 6\pi w^2$, $\text{adapt_thresh} = 2w$, $\text{glob_thresh} = 2\sigma$ above sky level, $\text{smooth_size} = 0.5w$, $\text{fill_hole_size} = 0.5w^2$, where w is the extraction scale (in pixels) and σ is the standard deviation noise level expected in the arctan-transformed, convolved images. We were guided in these decisions by the discussion of methodological testing included in Koch & Rosolowsky (2015) and the online FILFINDER code tutorial/test suite. The specific choice of parameters has minimal influence on the resulting filament masks but this will be quantified fully in a follow-up paper analyzing the entire set of PHANGS–JWST targets. One particular planned aspect of expanded testing is benchmarking in the multiscale extraction regime. Such a future study will also ideally include JWST-based comparison of FILFINDER to other codes for filament extraction (e.g., Sousbie 2011; Men’shchikov 2021a, 2021b; Alina et al. 2022; Carrière et al. 2022). Note, however, that FILFINDER has been successfully utilized for astrophysical analysis in many works and in some instances compared to other codes (e.g., Green et al. 2017).

In addition to the filament masks generated for extraction at specific scales, we also produce masks representing the union of filaments detected cumulatively at different scales. For these cumulative masks, we sum the individual masks (for scales less than or equal to the current scale) and then flatten the result, such that it has a value of 1 anywhere a constituent scale contributes filament coverage. The cumulative summed mask before flattening is also retained, as it highlights the multiscale nature of the filament network. The Appendix presents individual scale and cumulative multiscale masks for F770W, F2100W, and HST B band as a Figure Set.

The wide range of scales initially allowed for filament extraction is exploratory. In the second half of Section 4.1, we argue that all emission and attenuation filament masks for scales >200 pc not be used, although we do include them in plots allowing for the reader to make their own judgment.

3.2. DFN Characterization

For Section 4.1, we measure the filament mask overlap categorizing each pixel as belonging to one of four classes: (1) attenuation filament only, (2) emission filament only, (3) both attenuation and emission filaments, or (4) no filamentary features detected. Note that the sight-line fractions we report in Section 4.1 for classes (1)–(3) are normalized to the total count of pixels with any detected filamentary feature, rather than the total count of pixels in the image. It is beyond the scope of the current study to quantify the dependence of pixel classes on the depth of the imaging—however, given the pervasive character of the detected filament network, we suggest that at least the F770W, F1000W, and F1130W observations are sensitive enough to make this a moot point. Our F2100W data are about $2\times$ less sensitive in absolute terms of limiting surface

brightness, σ_1 [MJy sr⁻¹], and also suffer from a similar loss in resolution compared to F770W. These factors likely contribute to the loss of some smaller-scale filamentary structure in the F2100W imaging.

Section 4.2 (flux fractions) requires the local estimation of the diffuse emission to obtain the background-subtracted filament flux. Methods of background determination are highly varied (e.g., circular annuli, region-hugging annuli, background surface determination) and generally selected on the basis of the specific use case. We employ the PHOTUTILS (Bradley et al. 2022) `background2D` code, supplying filament masks to indicate which pixels the procedure should ignore. A mesh of bins (each having a size two-thirds of the filament extraction scale) is defined, and the mode of unmasked pixels is determined in each bin. These mesh modes are median-filtered with a 3×3 boxcar (ignoring bins with too many pixels masked as within a filament), and the resulting values are interpolated across the image grid. Finally, the `background2D` output is subtracted from the input image, and nonfilament pixels are set to zero. Integrating this result gives the background-subtracted flux of the filament structures, which is then divided by the total flux in the MIRI footprint to obtain flux fractions.

4. Results

Figure 1 illustrates the dust lanes seen as deficits of visible light (left) and dust emission filaments detected in MIR emission (right). Plotted for a single extraction scale (25 pc), the central panel emphasizes the detailed coincidence between these two tracers of dust (blue = attenuation, red = emission) in the interstellar medium, with magenta indicating overlap. It is clear that the DFN occupies a large fraction of sight lines and contributes a significant fraction of the MIR luminosity of NGC 628. Knots of emission from star-forming regions are generally distributed throughout the filaments. In this section, we quantify each of these statements.

Here we show results only for F770W and F2100W, as the filament masks and measured quantities based on F1000W and F1130W are consistent with F770W. Any notable differences are discussed.

4.1. Contrasting Views of the Dust Filament Network

We start by highlighting the consistency between filamentary attenuation (dust lane) features and web-like MIR dust emission to illustrate the potential of using HST-detected features as a high-resolution proxy for the dense dusty ISM morphology (and perhaps even molecular gas⁴²).

Figure 2 shows the results of filament overlap analysis. For the PAH-dominated bands (F770W, F1130W) and $10 \mu\text{m}$ thermal emission traced by F1000W, in the top panel of Figure 2, we find that the percentage of sight lines in common between visible attenuation and MIR emission filaments is nearly 40% at 25 pc and declines smoothly with increasing scale (filament width). This decline is due to more area becoming traced by attenuation only for larger individual filament extraction scales. The percentage of emission-only filament sight lines declines a small amount from 25 to 200 pc. Overlap statistics generated on the basis of cumulative multiscale masks show a different picture, in which the

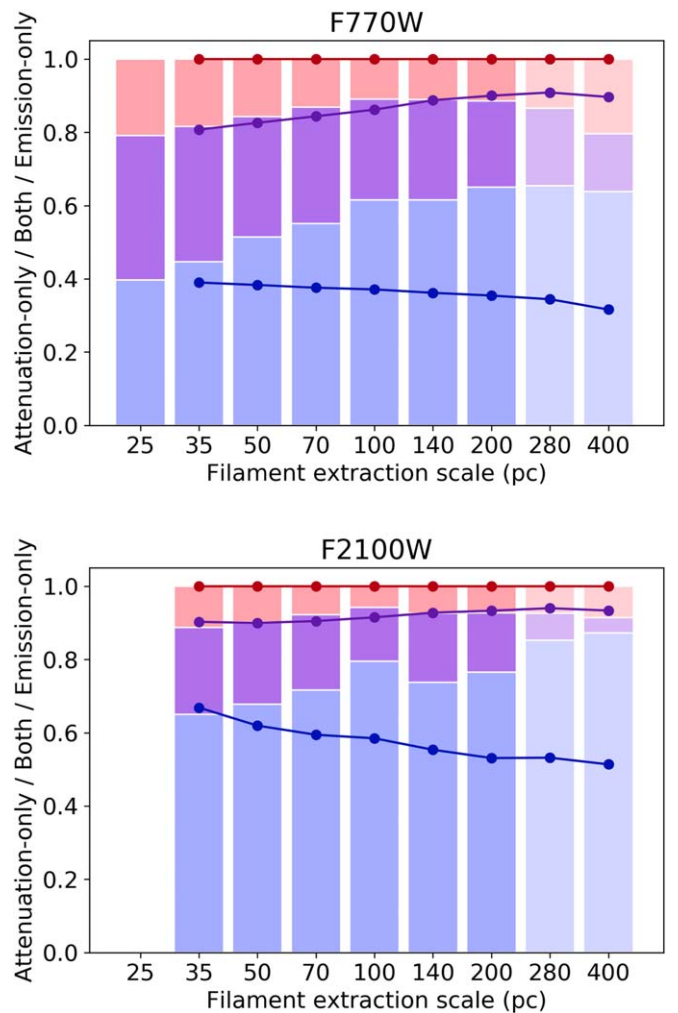


Figure 2. Filament overlap analysis for structures traced by visible attenuation and by MIR dust emission, as a function of extraction scale. Blue markings represent sight lines with attenuation only, magenta markings represent areas of overlap of between attenuation and emission, and red markings account for sight lines with emission only. Top: F770W. Bottom: F2100W. Results generated for cumulative masks are shown with points and sloping lines. We disregard scales >200 pc (shown faded in the plot) because the filament masks become unreliable (in the case of attenuation) or redundant with smaller-scale features (for emission). The first bar of the F770W plot (25 pc) presents the measurement for masks shown in Figure 1.

percentage of attenuation plus emission sight lines grows with scale from just over 40% at 35 pc to 55% up to 200 pc. This is a consequence of different extraction scale masks picking up varied portions of the overall web-like DFN. We return to this point further in the current subsection (see Figures 4 and 5).

In the bottom panel of Figure 2, we show the overlap for F2100W emission filaments with the dust lanes from HST. At $21 \mu\text{m}$, the percentage is 24% for 35 pc individual extraction scale, substantially less than for the three other bands, declining to $\sim 16\%$ for 200 pc. For all separate scales, attenuation-only sight lines amount to more than 65% and emission-only $\lesssim 10\%$. Given that the attenuation filament mask remains constant in comparison to F770W and F2100W, this could suggest that either we are sensitivity limited for F2100W or the filamentary emission detected in $21 \mu\text{m}$ imaging is less consistently recovered into coherent structures. The latter interpretation is supported by mask inspection in the figures of the Appendix and by the fact that the morphology of the F2100W image is

⁴² The association between the DFN structures and $^{12}\text{CO}(2-1)$ -traced molecular gas will be investigated in a future study.

more dominated by compact sources (e.g., IR-bright star-forming regions; see Hassani et al. 2023, this Issue) than F770W, F1000W, and F1130W. This serves as a reminder that we are tracing warm (140 K) dust at 21 μm , whereas the dust attenuation provides a more complete inventory with respect to dust over a wide range of (cooler) temperatures. Nevertheless, the overlap with the 200 pc cumulative multiscale mask is 40% (only $\sim 1/3$ less than for F770W).

In summary, the 40% level of pixel-by-pixel agreement of the attenuation and emission filament masks at 25 pc and the trend for the greatest agreement on the smallest scales suggest that the correspondence may be even tighter if smaller physical scales are probed, such as in Local Group galaxies. We stress that although 40% overlap may sound low, inspection of Figure 1 shows that the detailed morphology (e.g., extent, shape) of filaments that are detected in attenuation and dust emission is frequently rather well matched. We also note that regions of the filament network only found as dust emission are expected due to line-of-sight effects: Some filaments will be positioned on the “back” side of the face-on galaxy disk and could account for the majority of “emission-only” areas. The attenuation-only regions could be explained in multiple ways. As noted above, the dust temperature distribution, but also grain size distribution and PAH fraction (Chasten et al. 2023a, this Issue, Chasten et al. 2023b, this Issue, Dale et al. 2023, this Issue, Egorov et al. 2023 this Issue), can influence the degree to which the MIRI bands are a complete tracer of the dust distribution. Some attenuation-only regions also lie in false negatives for MIR dust emission on the scale of interest or lie in relatively MIR-faint, intermediate-surface-brightness regions of the visible galaxy disk. False negatives occur when an MIRI filament structure has a width that is somewhat different than the visible attenuation feature or when scale-matched emission in the region is biased against detection at the scale of interest (e.g., a filament centered between brighter neighboring emission features spaced by about the width of the FILFINDER adaptive thresholding box).

One might wonder if segmenting the galaxy into filaments is actually necessary or if it might be just as useful to characterize the level of correlation between emission and attenuation with a pixel-level scatter plot between the two quantities. As described in Section 5, such analysis will be included in future work, but even then the estimation of attenuation will require division into filament and nonfilament regions unless the properties of the local stellar population behind (or mixed with) the dust is otherwise known. Furthermore, the focus of the present paper on filament morphology/overlap and the association with star formation activity requires segmentation.

Figure 3 shows the division of sight lines between those associated to a dust filament (here, either attenuation or emission) and those that do not lie in a filament for the particular extraction scale. The plots show very little change between bands. We find that approximately 50%–55% of sight lines are attributed to dust filaments for scales 25–100 pc with no variation due to extraction scale, then a mild increase at larger scales (to $\sim 60\%$ – 65% for 200 pc). Cumulative multi-scale mask measurements of the dust filament sight-line fraction (dots and lines in Figure 3) steadily rise across the 25–200 pc range, despite the constancy for individual extraction scales smaller than 140 pc. Our filament masks are detecting a morphologically diverse dusty ISM, with features ranging from very narrow filaments like the Milky Way’s

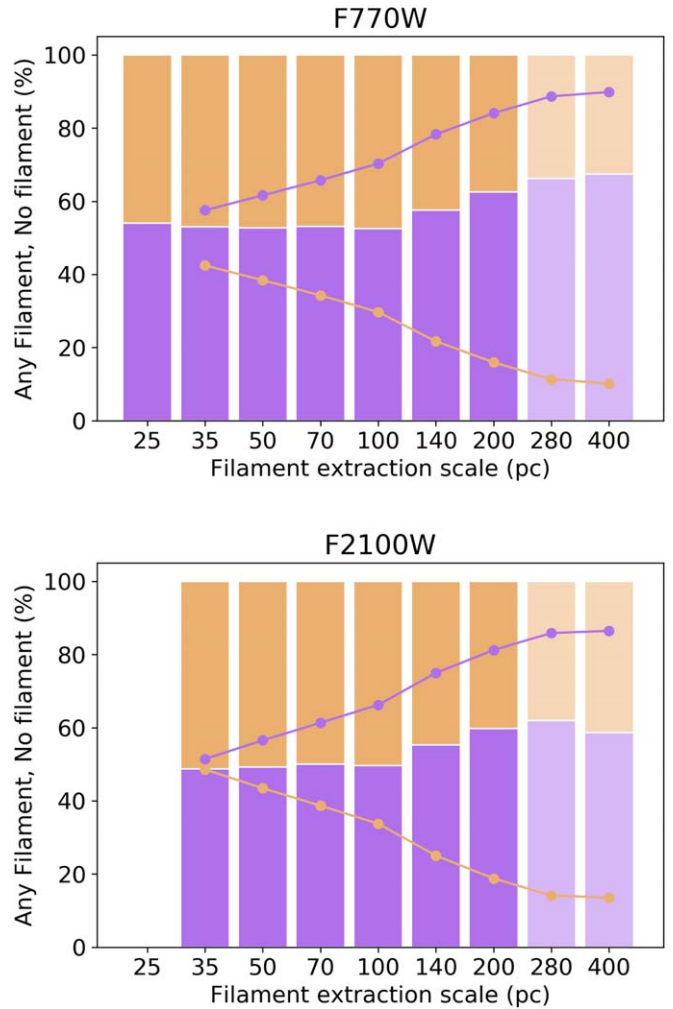


Figure 3. Areal coverage of dust filaments. Top: for F770W, the fraction of pixels covered by a dust filament mask (emission or absorption) or left unassigned to a dust filament. Scales we elect to exclude from the filament network (see text) are shown faded in the plot. Bottom: same, for F2100W.

“bones”/“Giant Molecular Filaments” to lower density, more diffuse dust filaments. Though beyond the scope of this paper, it will be important to investigate if the latter component is increasingly atomic-dominated compared to narrower filaments.

Figure 4 illustrates the tendency for dust filament masks to capture different morphological features when extracted using varied scales. In particular, we show the JWST F770W image in the top panel and the HST *B* band in the bottom panel. Using red and blue lines, overlotted on each of the images is a contour boundary of the 25 pc mask (dashed thin line) and 200 pc mask (solid thick line), with the variety of mask corresponding to the dust detection property of each image (emission on top, attenuation on bottom). Many of the single extraction scale 25 pc dust filaments are very long, with $l > 1$ kpc and have a rather high aspect ratio. However, there are also frequent cases of the 25 pc masks (dashed thin lines) only including localized substructure within larger coherent filaments left unjoined by small-scale extraction. This selective property of the filament identification outcome can be seen in spiral arms (markedly less so in interarm regions) and in both emission and attenuation. Conversely, the 200 pc filament

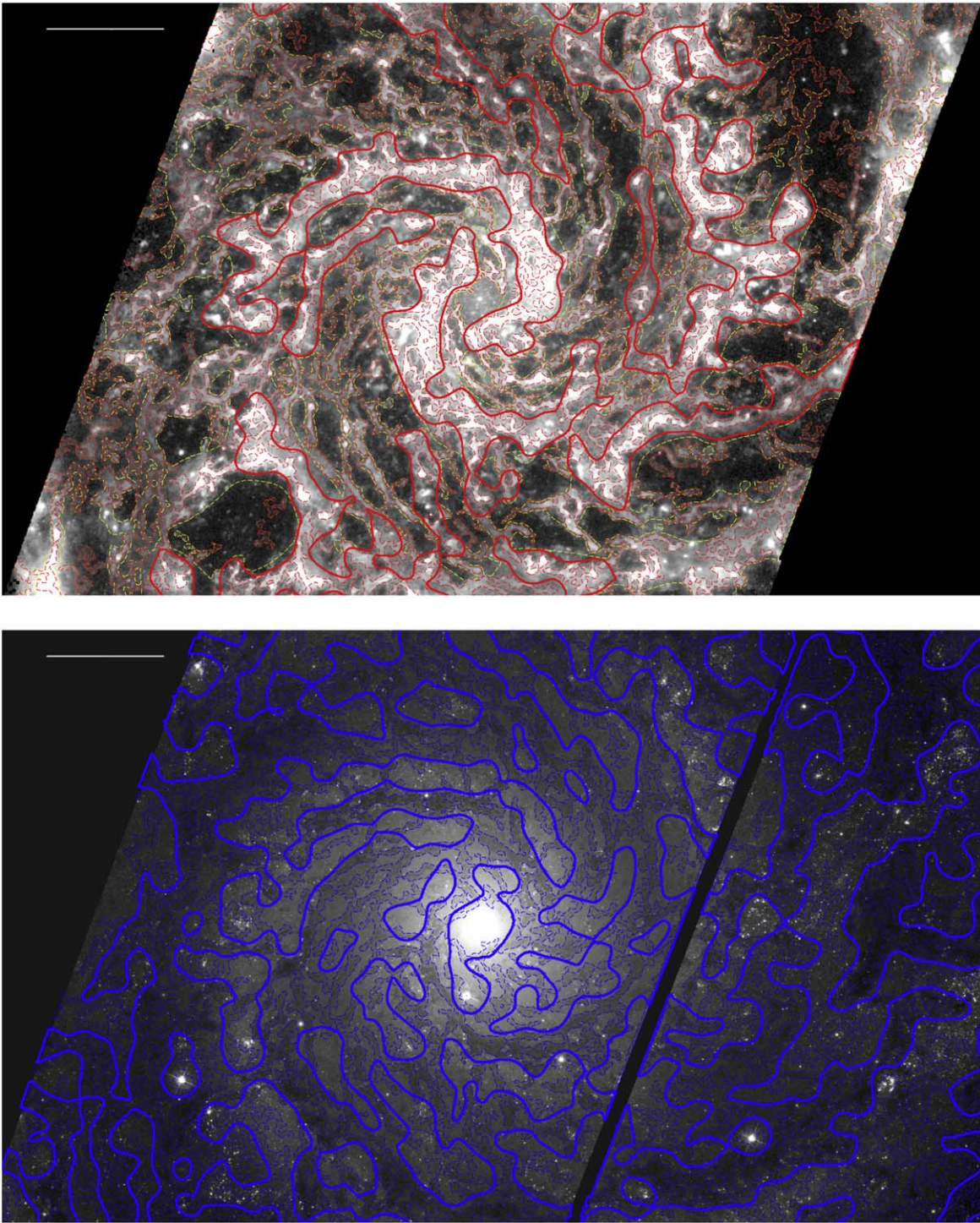


Figure 4. Contrasting filamentary dust structures in NGC 628 as seen in emission and attenuation, with emphasis on features identified at varied filament extraction scale. Top: JWST F770W image. Dust emission filament mask boundaries are shown for 25 pc dashed, thin red; 200 pc, thick red; and cumulative 400 pc, dashed thin yellow. Bottom: *B*-band F435W HST image, with attenuation filament mask coverage of 25 pc dashed, thin blue; 200 pc, thick blue. The scale bar in each panel is 1 kpc in length, and the images are oriented north up and east left.

masks (solid thick lines) often entirely exclude areas with a significant population of narrow GMC-scale width filaments. We note that the 200 pc attenuation filament mask recovers continuous spiral structure more effectively than the F770W emission mask of the same scale. Additionally, Figure 4 demonstrates that the recovered dust attenuation features can be quite modest in terms of apparent $A(B)$. Inspection in the peripheral areas of the HST panel nevertheless suggests the

majority of such filaments are real. On the JWST image, we also plot a contour representing the cumulative (up to 400 pc) emission filament mask (dashed thin yellow). The 25 and 200 pc filament structures alone do not include all portions of the DFN, especially in dust emission. The yellow contour shows how using a cumulative mask addresses this issue, linking many smaller-scale components. Using cumulative masks with large upper scales can excessively broaden the

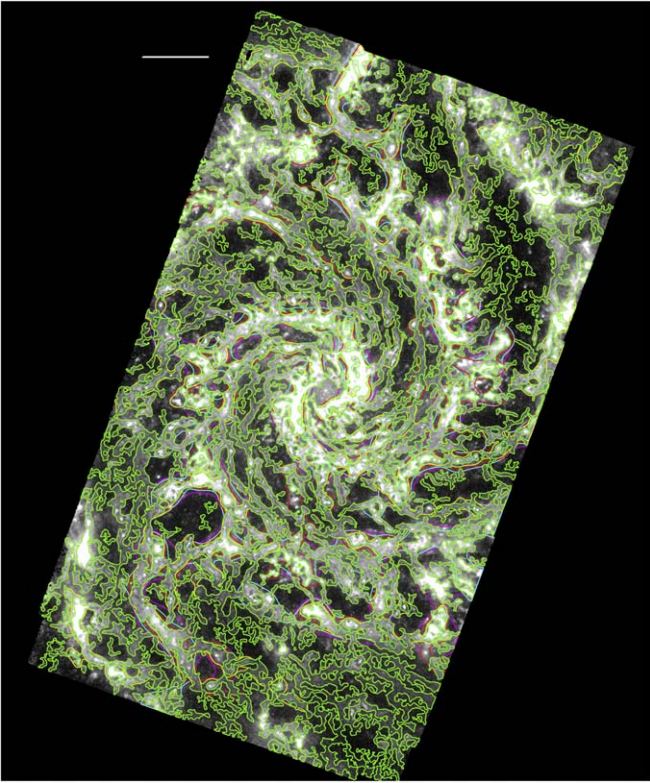


Figure 5. Comparison of cumulative filament masks up to varied maximum scale. JWST F770W image of NGC 628, overplotted with the contours showing the coverage of multiscale masks. The maximum scale is as follows: green, 100 pc; yellow, 140 pc; red, 200 pc; cyan, 280 pc; magenta, 400 pc. We adopt 200 pc as a preferred value. The scale bar corresponds to 1 kpc, and the images are oriented north up and east left.

extent of filaments, and hence we urge caution in the choice of the upper limit on multiscale integration.

Figure 5 provides the empirical justification for maximum scale on the basis of emission. The figure plots the cumulative F770W mask boundaries for different maximum scales, starting at 100 pc (green), running through 140, 200, 280 pc (yellow, red, cyan), up to 400 pc (magenta). The top layer contour (100 pc, green) already encapsulates the majority of the overall structure of the DFN, but several regions of seemingly contiguous filamentary emission remain disconnected either internally or to the network. By looking at other colored contours emerging from under the green boundary, one can infer how adding progressively larger scales changes the network. The 200 pc cumulative mask (red) appears to provide reliable recovery of all filamentary emission structures without undue peripheral excess, although 140 and 280 pc are probably also acceptable. HST *B*-band filament extraction at 280 and 400 pc occasionally confuses interarm gaps as attenuation. Such large (>200 pc) scales also push the limit of what can be considered a filament in the sense of forming via turbulent Jeans scale gravitational instabilities (see Meidt et al. 2023, this Issue).

Figure 6 presents a zoomed-in view of a region east-southeast of the galaxy center, showing the filtered *B*-band data in comparison to an unprocessed version of the same image and to F1000W data from JWST. Contours of the 25 pc *B*-band and F1000W filaments are overplotted. This figure visually emphasizes the 40% sight-line overlap and morphological agreement at this scale. Figure 6 also demonstrates the

feasibility of probing even smaller scales in visible dust lanes across the entire PHANGS–HST sample. Significant substructuring (down to the ~ 5 pc WFC3/UVIS resolution limit in NGC 628) in attenuation of the features detected as dust emission filaments at 25 pc scales is apparent. We further expect HST to detect additional small-scale filaments beyond the limit of MIRI—several super-narrow attenuation filaments without corresponding larger-scale intensity depressions are apparent in other regions of NGC 628. Finally, Figure 6 demonstrates that with HST we will be able to reveal candidate features we nickname “dust motes” (examples marked with yellow circles), essentially compact ($\lesssim 10$ pc), dark clouds we cannot cleanly identify solely with JWST due to confusion with point-like dusty extreme AGB stars (D. A. Thilker et al. 2023, in preparation) lying outside the emission filament network (examples marked with green circles) in the short-wavelength MIRI images. These dust motes could be individual molecular clouds in relative isolation. Their size is comparable to the Taurus Molecular Cloud, although Taurus is star-forming whereas the motes may often be quiescent. A better Milky Way analog might be the smallest-scale clouds found in the 3D extinction maps of, e.g., Leike et al. (2020). Dust mote clouds are challenging to confirm with MIRI, but appear in the HST *B*-band images before any preprocessing (Figure 6 center). PHANGS–JWST F335M $3.3\ \mu\text{m}$ PAH imaging (Rodriguez et al. 2023, this Issue; Sandstrom et al. 2023a, this Issue) and forthcoming PHANGS–HST $\text{H}\alpha$ imaging (GO 17126, PI R. Chandar) may prove useful to further vet dust mote candidates as a class.

4.2. Fraction of Flux in the MIR Filament Network

The relative amount of structured and unstructured (diffuse) dust in a galaxy is a fundamental metric of ISM morphology and offers a basis for comparison with simulations that aim to understand the impact of factors such as stellar feedback and dynamical influences (e.g., Smith et al. 2020). As noted in Section 4.3, this observable is also relevant to star formation rate (SFR) estimation. We measure the fraction of flux contained within the extracted filaments compared to the total flux in the image. As the filaments are brighter than their surroundings, this requires that we establish a local background estimate at all locations in the image, which we do using the procedure given in Section 3. Figure 7 presents our results concerning flux fraction as a function of filament extraction scale.

We find that at the smallest independent extraction scales considered (25 pc for F770W, F1000W, F1130W; 35 pc for F2100W), the background-subtracted filament flux fractions are nearly 30% except for F2100W at $\approx 20\%$. The flux fraction is essentially constant versus the extraction scale for F770W, F1000, and F1130W, but peaks at 35 and 200 pc for F2100W. The F2100W flux fractions are always significantly less than all three shorter-wavelength MIRI bands. Given the present residual $\pm 0.1\ \text{MJy sr}^{-1}$ uncertainty in the background level of our MIRI images (see Section 2.1 and Leroy et al. 2023, this Issue), we assess the impact this has on filament flux fractions by offsetting the image intensities by the uncertainty in a positive and negative sense. Dashes overplotted on the bars of Figure 7 indicate the resulting perturbed fractions.

Cumulative multiscale mask filament flux fraction results are also shown in Figure 7, indicated by the solid lines and dots. As expected, the fraction increases as progressively more

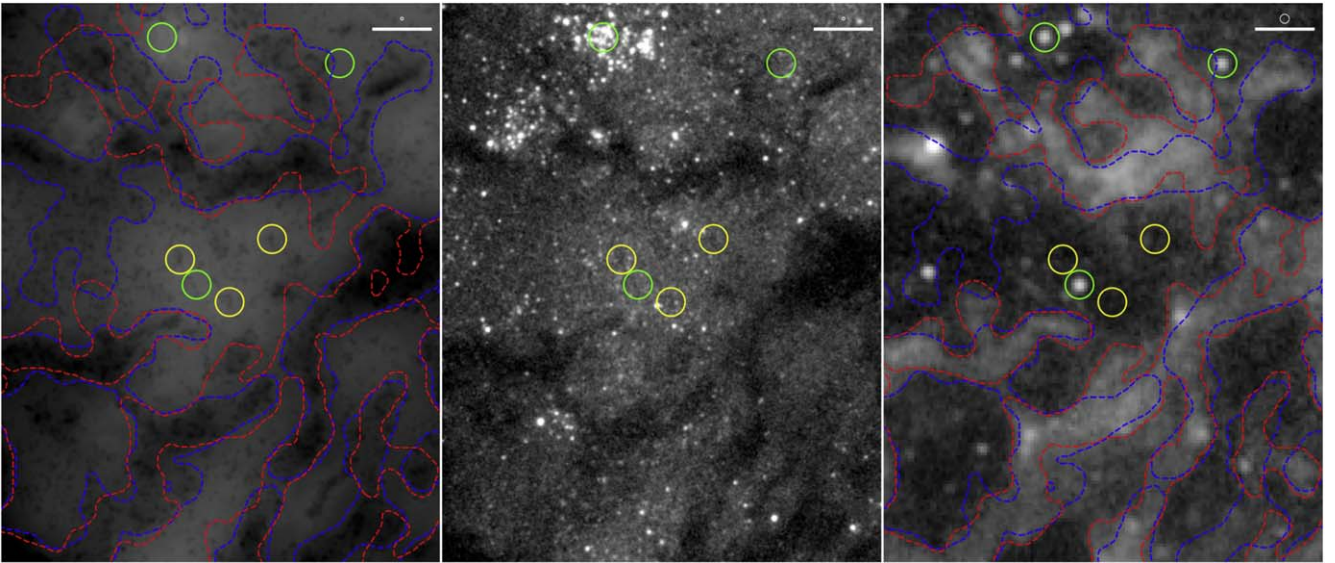


Figure 6. Dust motes and point-source MIR contamination from extremely dusty stars. Left: subsection of our preprocessed B -band image, overlaid with contours corresponding to the filament masks generated at 25 pc resolution in emission, red, and absorption, blue. Center: unprocessed B -band image. Right: JWST F1000W image, also with the filament mask contours shown. Yellow circles surround three example dust motes. There are many more in the field shown, left unmarked. Green circles surround three example candidate dusty stars, others are not marked. Circles are $1''$ in diameter, equivalent to 48 pc at the distance of NGC 628, and the images are oriented north up and east left.

individual masks are combined and the maximum allowed extraction scale is increased. For our choice of maximum scale (200 pc) the background-subtracted filament flux is in the range of 55% to 60% of the total F770W, F1000W, and F1130W flux in the field. At the same cumulative scale, the F2100W measurement is 43%. Scatter due to uncertainty in background level is also checked for cumulative values and shown with dotted lines on Figure 7. The impact is notably larger than for individual scales but is generally less than the systematic uncertainty due to our choice of maximum scale included in the DFN cumulative mask.

We note that if diffuse emission is ignored, rather than subtracted away as in our analysis, the integrated flux from the filament network becomes 40%–100% higher, boosting the cumulative filament flux fractions to $\sim 80\%$ for F770W, F1000W, and F1130W and 60% for F2100W.

4.3. Linking the Dust Filament Network to Star Formation Activity

The results of Section 4.2 confirm that more than half of the MIR flux from NGC 628 originates in the intricately structured filament network, with the only exception being for F2100W (43%). This outcome is what we anticipated based on previous work for nearby galaxies (Liu et al. 2011; Leroy et al. 2012; Calzetti 2013; Crocker et al. 2013; Boquien et al. 2016; Kumari et al. 2020; Belfiore et al. 2022). It reinforces the necessity of correcting the integrated MIR luminosity of a galaxy for the presence of inherently diffuse emission heated by older stellar populations when using MIR to measure the current SFR (Lonsdale Persson & Helou 1987; Boquien et al. 2016). One of the goals of PHANGS–JWST is to clarify systematics of this correction. We can positionally test the linkage of the DFN to age-dated markers of star formation events, checking whether all regions of the filament network can be attributed to heating by current star formation or if some filamentary structure is effectively quiescent and should be removed alongside diffuse emission when estimating SFR. Put differently, perhaps only

filamentary structure up to a certain maximum scale, or down to a limiting dust surface density, is directly linked to the youngest stellar populations.

We take a first step toward the goal above by cross-correlating the filament masks with the PHANGS–MUSE H II regions, plus PHANGS–HST young (≤ 5 Myr) clusters and associations, described in Section 2. With these populations, we measure unweighted inclusion fractions (number of objects contained within the filament mask divided by the total count in the image footprint) and also tracer-weighted inclusion fractions (summing weights corresponding to SFR rather than object counts). For weighting we use extinction-corrected L ($H\alpha$), effectively unobscured SFR, for H II region populations; and $M_*/\text{age} \approx \text{effective SFR}$ (5 Myr) for young clusters and associations.

Figure 8 plots the measured inclusion fractions for each of the test populations. As a control, we also evaluated band- and scale-dependent inclusion fractions (and their standard deviations) obtained for many sets of randomized positions in the footprint. Figure 8 shows the randomized fractions in the top two panels. We begin by making general comments about Figure 8, which are applicable to all panels. We find that the inclusion fractions (at individual scales or cumulatively) are consistently maximized for H II regions but decline slightly when using young clusters and dramatically using young associations, regardless of scale or band. The inclusion fraction measured at individual filament extraction scales for H II regions and young clusters (≤ 5 Myr) decline from a maximum at 25 pc until reaching 70–100 pc. For associations, there is a far weaker, if any, dependence on scale over the same range, but an apparent enhancement at 140–200 pc scales. The random inclusion fractions for unweighted measurements (top panels) provide further insight. They indicate strong correlation between dust emission filaments and H II regions/young clusters, moderate anticorrelation of associations with filaments at scales < 100 pc, and increasingly strong correlation of associations with the DFN for extraction scales of 100, 140,

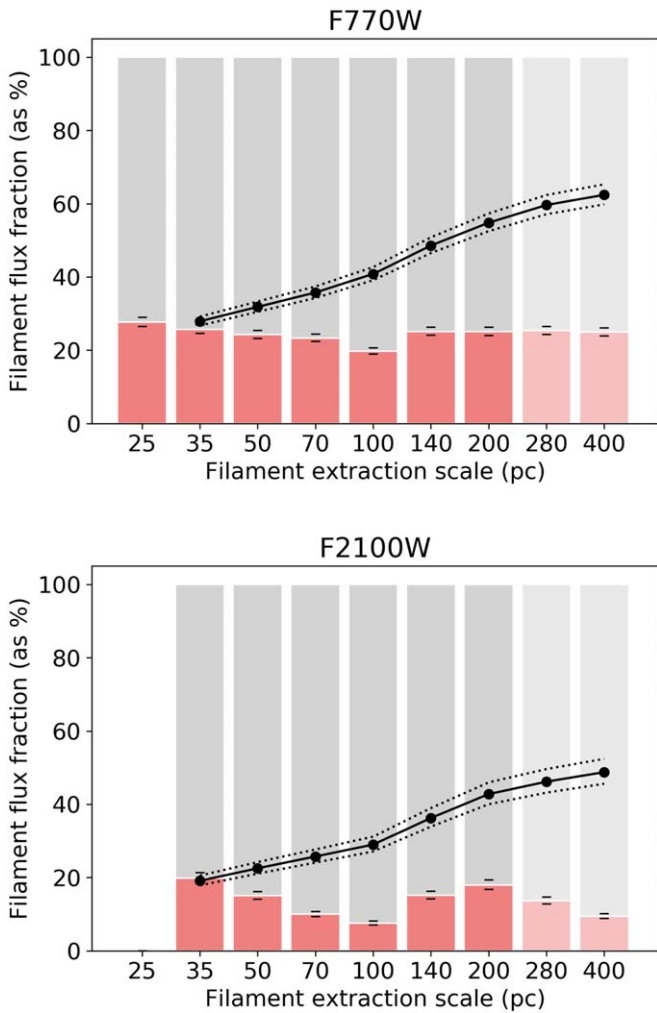


Figure 7. Measurements of the fraction of total flux contained within the DFN. Top: filament flux fraction in F770W expressed as percentage, with individual filament extraction scales plotted as pink bars and cumulative multiscale results as solid lines and points. The faded region is shown for completeness, although we adopt a maximum cumulative scale of 200 pc. Horizontal dashes on each bar indicate the 1σ uncertainty of the flux fraction measurements, obtained by perturbing the sky level in accordance with the postpipeline calibration described by Leroy et al. (2023, this Issue) and Lee et al. (Lee 2023, this Issue). Dotted lines show the 1σ range due to the uncertainty of cumulative flux fractions. Bottom: same, but for F2100W.

and 200 pc. For measurements made with cumulative masks, the inclusion fractions (unweighted and weighted) increase with scale as would be expected. The slope of the cumulative curves in Figure 8 (top) is consistent with the scale dependence of the randomized control, showing the influence of significant multiscale mask-covering fraction, but normalization is significantly higher (excess over random $20\sigma \pm 5\sigma$ for H II regions, 3σ – 6σ for young clusters) except for associations. For associations, the small-scale signal of anticorrelation dominates until our cumulative measurement finally reaches random equivalence by 200 pc.

The SFR-weighted inclusion fractions (Figure 8, bottom) are perhaps more physically relevant to the questions raised at the start of this section. Remarkably, our measurements show about 75% of the SF traced by H II regions is occurring within the 25 pc scale of the F770W filament network (bottom left), whereas the peak SFR-weighted inclusion fraction for F2100W is $\sim 45\%$ (at 35 pc, bottom right). We find the single-scale SFR-

weighted inclusion fractions are highest overall for F1130W and F1000W at nearly 80% for the 25 pc filament extraction (not shown). Perhaps the most striking measurement linking the dust emission filaments to current star formation is the attainment of $\sim 95\%$ SFR-weighted inclusion by our uppermost cumulative scale, 200 pc, for each of F770W, F1000W, and F1130W when using the multiscale masks, and 72% for F2100W. Our finding of decreased inclusion fractions for F2100W agrees with the assessment of the relative suitability of MIRI bands as a gas column density tracer by Leroy et al. (2023, this Issue) and Sandstrom et al. (2023b, this Issue), which show that the PAH-dominated bands are preferable to F2100W as a high-resolution proxy for gas.

We anticipated seeing a reduction in inclusion fraction for stellar associations, since, although the associations are young, they are star formation events that have evolved from clusters via disruption/dissolution or were initially formed unbound, and either way seem more likely to have already cleared their environment of dust. However, the anticorrelation observed at small scales is an unexpected demonstration that such feedback actively helps to sculpt the dust into bubble/shell structures (e.g., Barnes et al. 2023, this Issue; Watkins et al. 2023, this Issue).

Work is currently underway to obtain a catalog of PHANGS–ALMA GMCs associated with embedded ($t \sim 0$ Myr) star formation, indicated by compact F2100W sources coincident with a GMC (R. Lessing et al. 2023, in preparation). When ready, we will compare our dust emission filaments to that population. We emphasize that the F2100W source population does not drive the identification of filaments at $21\ \mu\text{m}$ due to FILFINDER’s transformation of the image intensity scale.

5. Summary and Future Work

This paper presents an initial exploratory analysis of PHANGS–JWST+HST imaging for NGC 628, revealing its extensive DFN as seen in both MIR emission and visible attenuation. Our pilot investigation offers insight into the extragalactic ISM structure at small scales rarely probed by other tracers, including atomic and molecular gas, with an emphasis on quantifying filaments and associated star formation activity.

Conclusions from our study are as follows:

1. At the smallest extraction scale currently considered (25 pc filament width), the agreement of independently constructed attenuation and emission filament masks is 40%. More so, the detailed morphology of filaments that are detected in both ways is frequently rather well matched with only minor deviations in shape or extent. We find evidence for emission-only filaments (and portions of filaments) likely on the “back side” of the galaxy disk, but also a less well-understood set of attenuation-only filaments that requires further characterization.
2. No single extraction scale (filament width) provides a complete inventory of all filamentary dust emission structures. Our structure masks are detecting a morphologically diverse dusty ISM, spanning from very compact GMC-sized filaments to larger-scale, lower-surface-brightness filaments ultimately constituting galactic spiral arm features. We anticipate that the molecular fraction

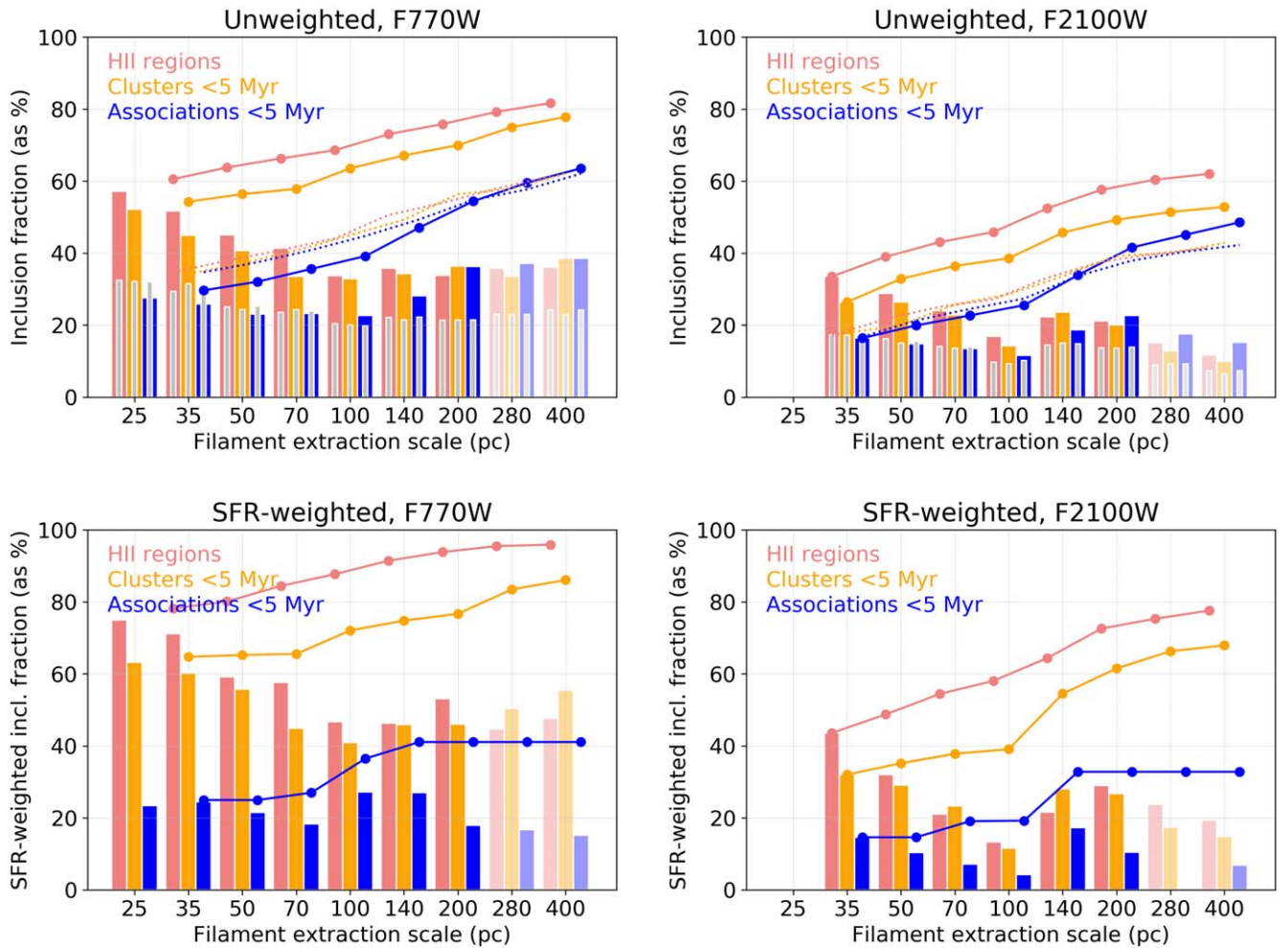


Figure 8. Testing the link of the DFN to current star formation. Top: filament inclusion fractions for various star formation event tracers (H II regions, young clusters, young multiscale associations) vs. the dust emission filament extraction scale. Bars indicate results for each individual extraction scale, whereas lines and points indicate the cumulative filament mask measurements. Inclusion fractions for randomly distributed points are shown with inset bars and dotted lines. Bottom: SFR-weighted inclusion fractions.

probably declines with increasing scale in this hierarchy but require higher-resolution observations of atomic gas in order to check this.

3. HST reveals candidate features we nickname “dust motes,” which are comparatively isolated (lying outside the DFN) and appear as compact ($\lesssim 10$ pc) dark clouds essentially unrecoverable with JWST/MIRI alone due to confusion with dusty stellar point sources. They could trace largely quiescent individual molecular clouds. Regardless of whether candidate “dust motes” are ultimately verified as a bona fide population, HST is capable of probing substructure in dust filaments at scales smaller than MIRI.
4. Approximately one-third of the total MIR flux in the F770W, F1000W, and F1130W bands are contained in the 25 pc scale mask of the emission filament network using diffuse background-subtracted measurements. The flux fraction determined for the 200 pc limited cumulative multiscale filament mask is 55%–60% in the same bands. The F2100W filament flux fractions are significantly less than the others, with a cumulative measurement of $\sim 45\%$. This is in line with Leroy et al. (2023, this Issue), who showed that F2100W correlates less well with CO

than the other MIRI bands and that it is not as clean of a tracer of column density.

5. Our filament inclusion fraction analysis shows that 75%–80% of the current star formation traced by H II regions is occurring within the 25 pc scale of the filament network. The analogous measurement for young (<5 Myr) clusters is slightly more than 60%. Integrated over cumulative scales up to 200 pc, the H II region fraction exceeds 95%. A similar analysis demonstrates the moderate anticorrelation of associations younger than 5 Myr with dust filaments at scales <100 pc then a reversal to increasingly strong association-filament correlation for extraction scales of 100, 140, and 200 pc.

Expansion and further development of our work to the remaining PHANGS–JWST galaxies will (a) provide clarity from an external and diversified perspective, which is absent from Galactic studies and which can allow quantification of trends in filament properties with local environmental physical conditions, (b) enable comparison to increasingly detailed simulations, which can isolate the effects of different ISM-structuring mechanisms, (c) constrain the dependence of opacity on dust grain properties, and eventually (d) firmly quantify the division of MIR emission between currently star-

forming and evolved stellar populations (related to the work of Belfiore et al. 2022), with complete accounting of unobscured and embedded star formation (Hassani et al. 2023, this Issue; Rodriguez et al. 2023, this Issue). The union of JWST and HST dust tracing also motivates targeting for focused high-resolution ALMA follow-up mapping of dense gas. We further emphasize that ngVLA and/or SKA is required to obtain sensitive HI imaging at the substantially better than 6'' resolution that is needed to constrain ISM phase changes within the filamentary structures we study.

We plan the following practical improvements to our work in the near term. Attenuation (dust lane) features will be identified on the basis of the complete multiwavelength PHANGS–HST data set and at sub-MIRI-resolution scales. Determination of attenuation, $A(V)$, as a function of position (e.g., Butler & Tan 2009; Viaene et al. 2017) within the filament network will be accomplished, allowing pixel-by-pixel correlation of emission and attenuation to be measured. We will study the integrated SED of the filament network versus scale and use FILFINDER capabilities to generate catalogs of filament substructures with measured properties (such as length, aspect ratio, curvature, flux, mass per unit length) plus molecular-cloud-linked quantities (velocity gradient, CO velocity dispersion, virial parameter) when a GMC is found to be cospatial. Such cataloged properties will be ripe for comparison to equivalent quantities measured from simulations. We will assess whether or not embedded star-forming regions tend to be located at the intersection of filament spines, as they do in simulations. Lastly, we will analyze ensemble characteristics such as those noted above of dust emission and attenuation filament network substructures versus physical condition metrics (e.g., Sun et al. 2022) of the local (\sim kiloparsec-scale) environment.

This work was carried out as part of the PHANGS collaboration. Based on observations made with the NASA/ESA/CSA JWST and Hubble Space Telescopes. The data were obtained from the Mikulski Archive for Space Telescopes at the Space Telescope Science Institute, which is operated by the Association of Universities for Research in Astronomy, Inc., under NASA contract NAS 5-03127 for JWST and NASA contract NAS 5-26555 for HST. The JWST observations are associated with program 2107, and those from HST with program 15454. Based on observations collected at the European Southern Observatory under ESO programmes 094.C-0623 (PI: Kreckel), 095.C-0473, 098.C-0484 (PI: Blanc), 1100.B-0651 (PHANGS–MUSE; PI: Schinnerer), as well as 094.B-0321 (MAGNUM; PI: Marconi), 099.B-0242, 0100.B-0116, 098.B-0551 (MAD; PI: Carollo) and 097.B-0640 (TIMER; PI: Gadotti). We acknowledge the usage of the SAO/NASA Astrophysics Data System.⁴³ D.A.T. acknowledges funding support from STScI via JWST-GO-02107.002-A. E.W.K. acknowledges support from the Smithsonian Institution as a Submillimeter Array (SMA) Fellow and the Natural Sciences and Engineering Research Council of Canada. J.M.D.K. gratefully acknowledges funding from the European Research Council (ERC) under the European Union’s Horizon 2020 research and innovation program via the ERC Starting Grant MUSTANG (grant agreement number 714907). COOL Research DAO is a Decentralized Autonomous Organization

supporting research in astrophysics aimed at uncovering our cosmic origins. E.J.W. acknowledges the funding provided by the Deutsche Forschungsgemeinschaft (DFG, German Research Foundation)—Project-ID 138713538—SFB 881 (“The Milky Way System,” subproject P1). M.C. gratefully acknowledges funding from the DFG through an Emmy Noether Research Group (grant number CH2137/1-1). M.B. acknowledges support from FONDECYT regular grant 1211000 and by the ANID BASAL project FB210003. T.G. W. and E.S. acknowledge funding from the European Research Council (ERC) under the European Union’s Horizon 2020 research and innovation program (grant agreement No. 694343). E.R. acknowledges the support of the Natural Sciences and Engineering Research Council of Canada (NSERC), funding reference number RGPIN-2022-03499. F. B. would like to acknowledge funding from the European Research Council (ERC) under the European Union’s Horizon 2020 research and innovation program (grant agreement No.726384/Empire) K.G. is supported by the Australian Research Council through the Discovery Early Career Researcher Award (DECRA) Fellowship DE220100766 funded by the Australian Government. K.G. is supported by the Australian Research Council Centre of Excellence for All Sky Astrophysics in 3 Dimensions (ASTRO 3D), through project number CE170100013. R.S.K. acknowledges financial support from the European Research Council via the ERC Synergy Grant “ECOGAL” (project ID 855130), from the Deutsche Forschungsgemeinschaft (DFG) via the Collaborative Research Center “The Milky Way System” (SFB 881—funding ID 138713538—subprojects A1, B1, B2, and B8) and from the Heidelberg Cluster of Excellence (EXC 2181-390900948) “STRUCTURES,” funded by the German Excellence Strategy. R.S.K. also thanks the German Ministry for Economic Affairs and Climate Action for funding in the project “MAINN” (funding ID 50002206). G.A.B. acknowledges the support from ANID Basal project FB210003. M.Q. acknowledges support from the Spanish grant PID2019-106027GA-C44, funded by MCIN/AEI/10.13039/501100011033. E.C. acknowledges support from ANID Basal projects ACE210002 and FB210003. S.D. is supported by funding from the European Research Council (ERC) under the European Union’s Horizon 2020 research and innovation program (grant agreement no. 101018897 CosmicExplorer). K.K. and O.E. gratefully acknowledge funding from DFG in the form of an Emmy Noether Research Group (grant number KR4598/2-1, PI Kreckel).

Facilities: HST, JWST, VLT:Yepun.

Software: ASTROPY (Astropy Collaboration et al. 2013, 2018), NUMPY (Harris et al. 2020), MATPLOTLIB (Hunter 2007), FILFINDER (v1.7.2; Koch & Rosolowsky 2015)

Appendix

Dust Filament Masks versus Band and Extraction Scale

To permit the examination of the extracted dust filaments with respect to the JWST and HST data, we present the filament masks as a figure set. They are displayed first for F770W (Figures A1, A2), then F2100W (Figures A3, A4), and lastly the HST *B* band (Figures A5, A6). We show the filaments as transparent colored areas on the associated JWST or HST image. For each band, we present all of the individual scale filament masks in order of increasing extraction scale, followed by the cumulative multiscale masks.

⁴³ <http://www.adsabs.harvard.edu>

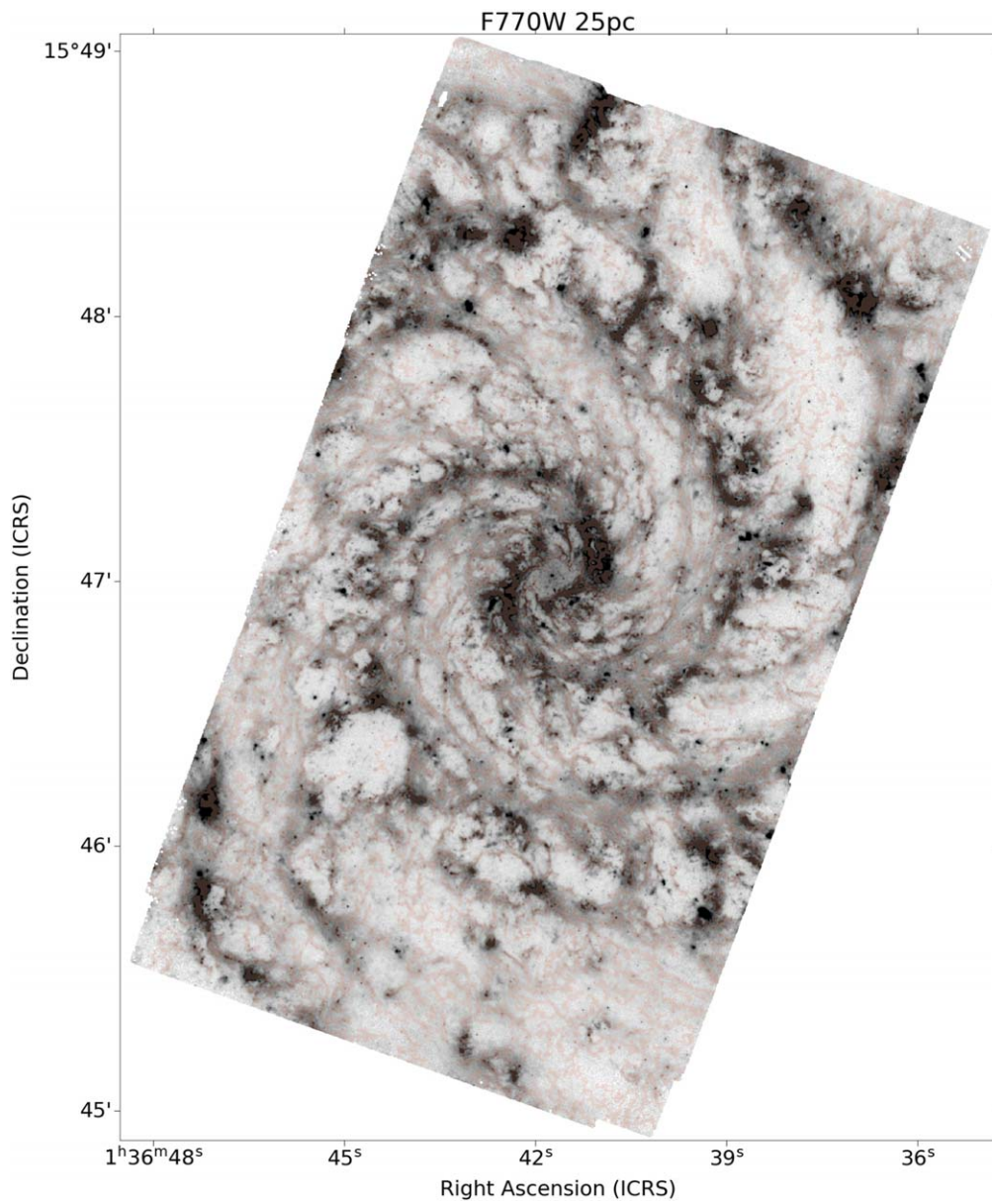


Figure A1. JWST F770W image with extracted emission filaments (25 pc scale) shown as transparent colored areas. The image is oriented north up and east left. (The complete figure set (44 images) is available.)

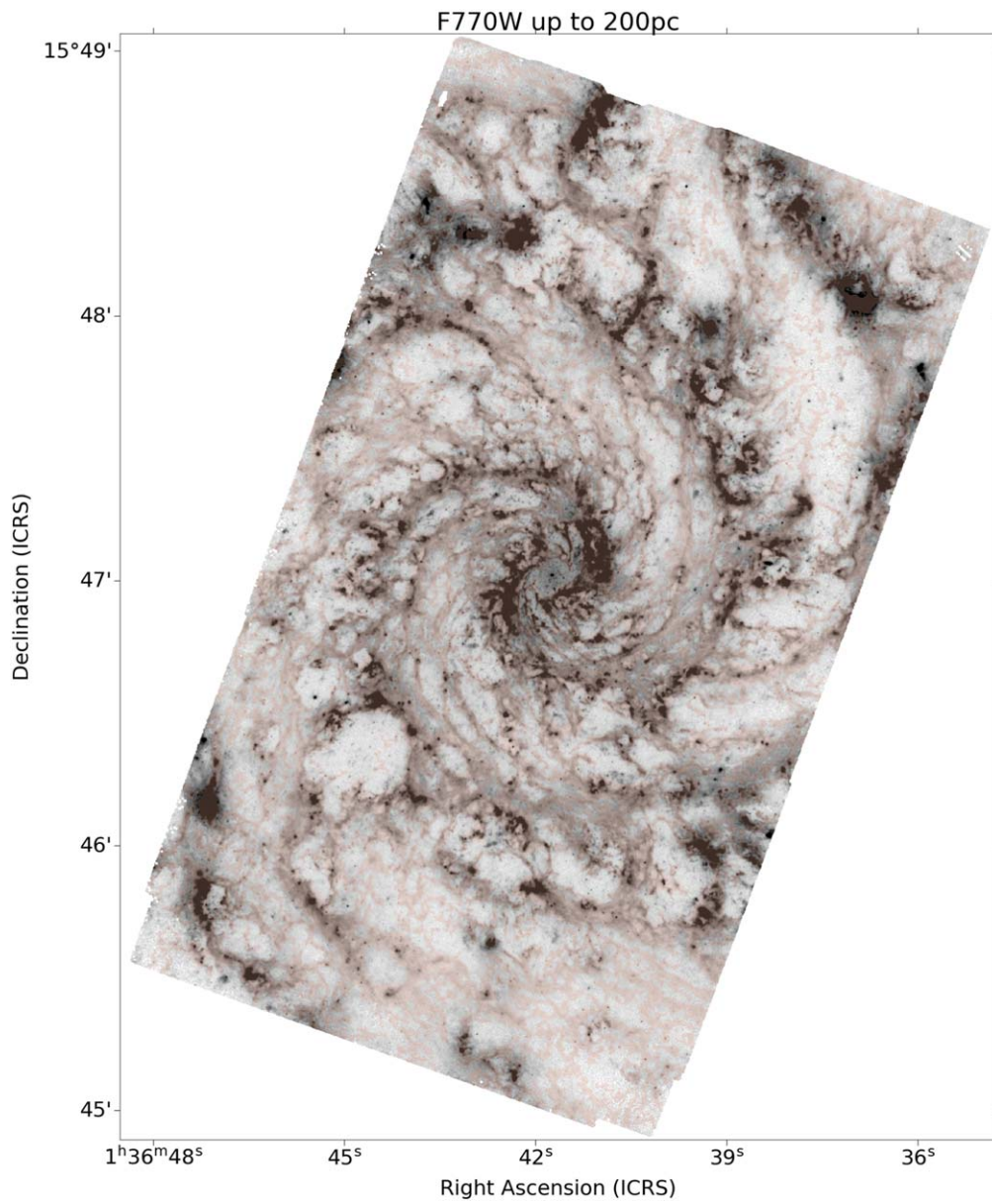


Figure A2. JWST F770W image with extracted emission filaments (cumulative up to 200 pc scale) shown as transparent colored areas. The image is oriented north up and east left.

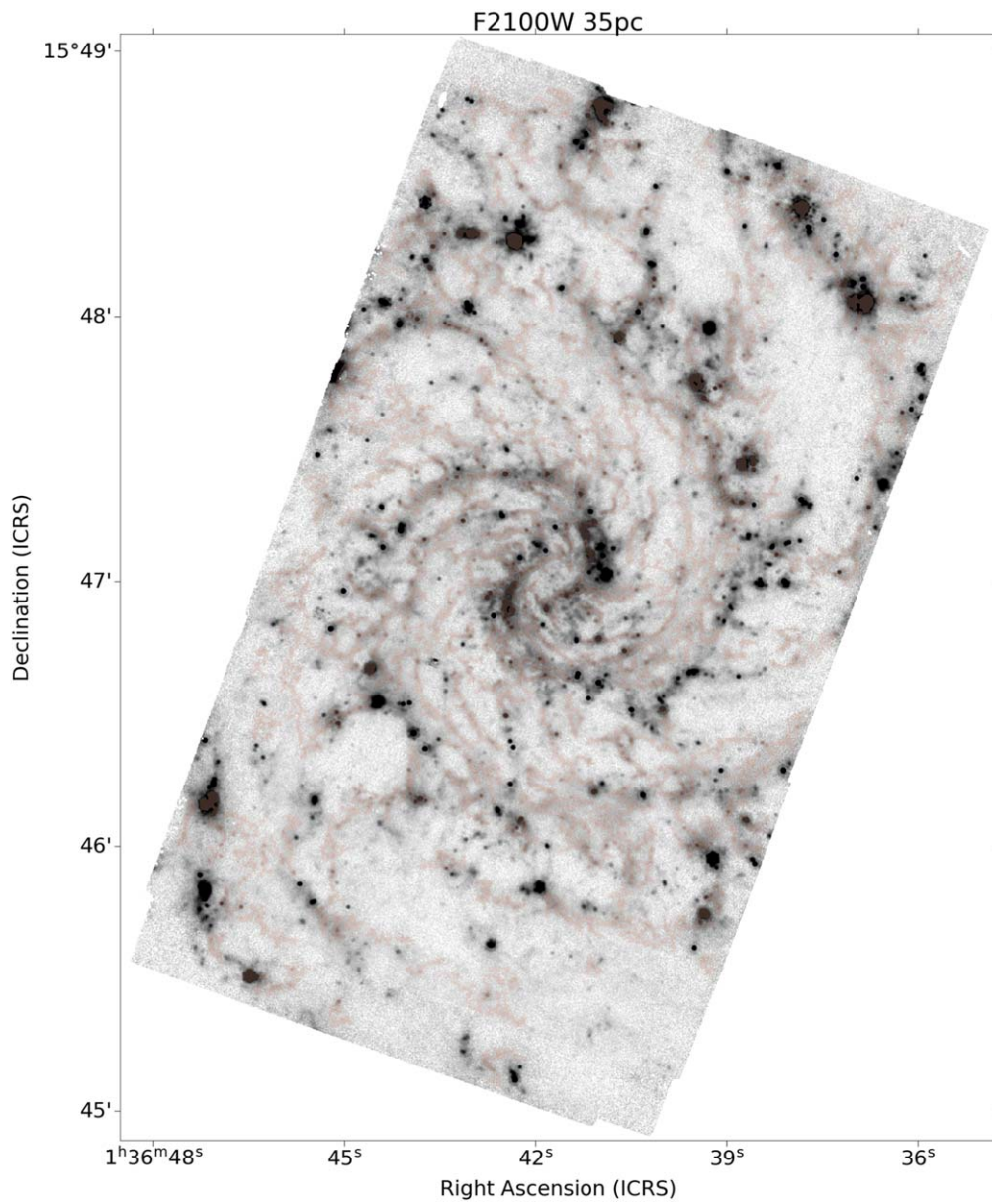


Figure A3. JWST F2100W image with extracted emission filaments (35 pc scale) shown as transparent colored areas. The image is oriented north up and east left.

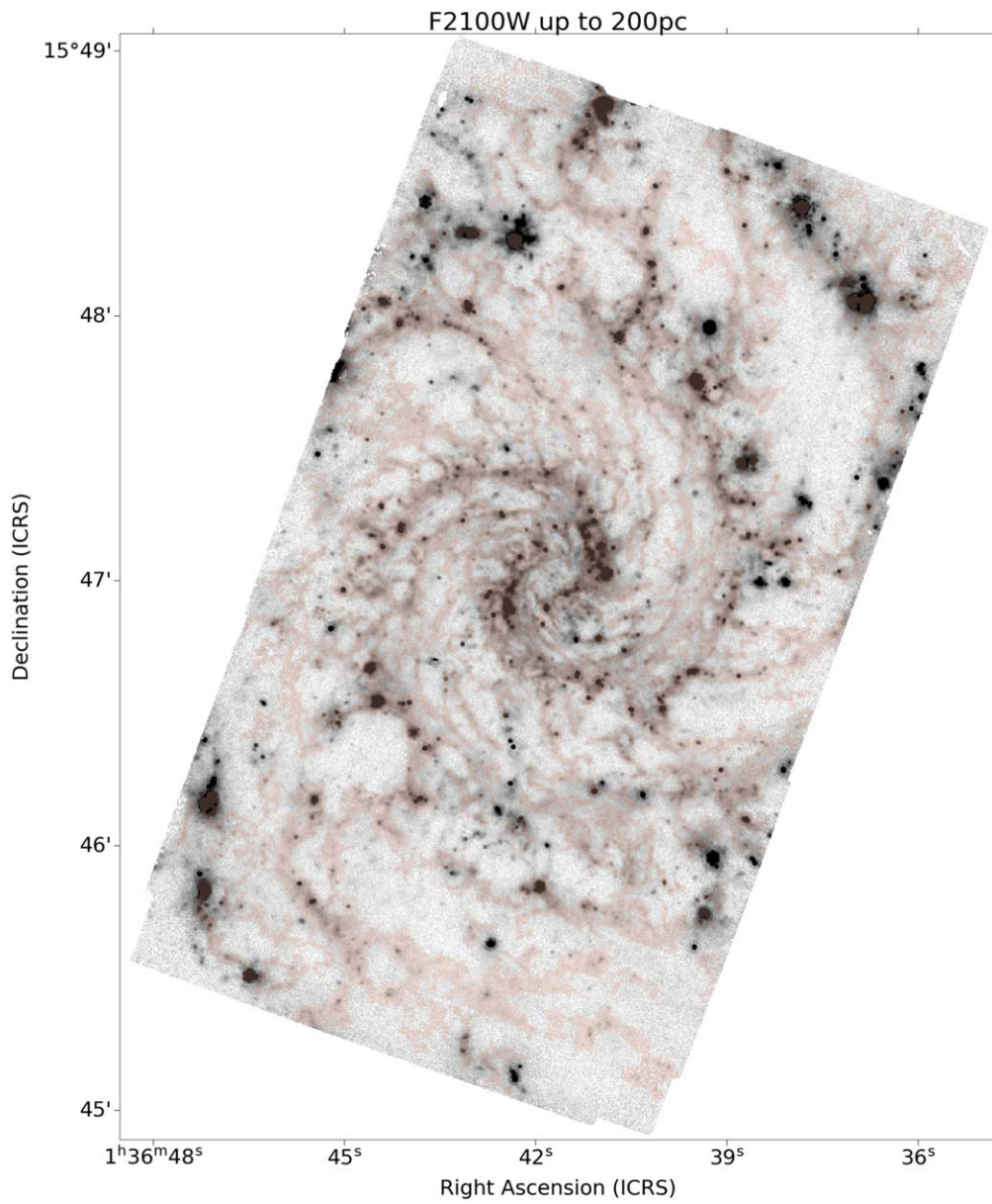


Figure A4. JWST F2100W image with extracted emission filaments (cumulative up to 200 pc scale) shown as transparent colored areas. The image is oriented north up and east left.

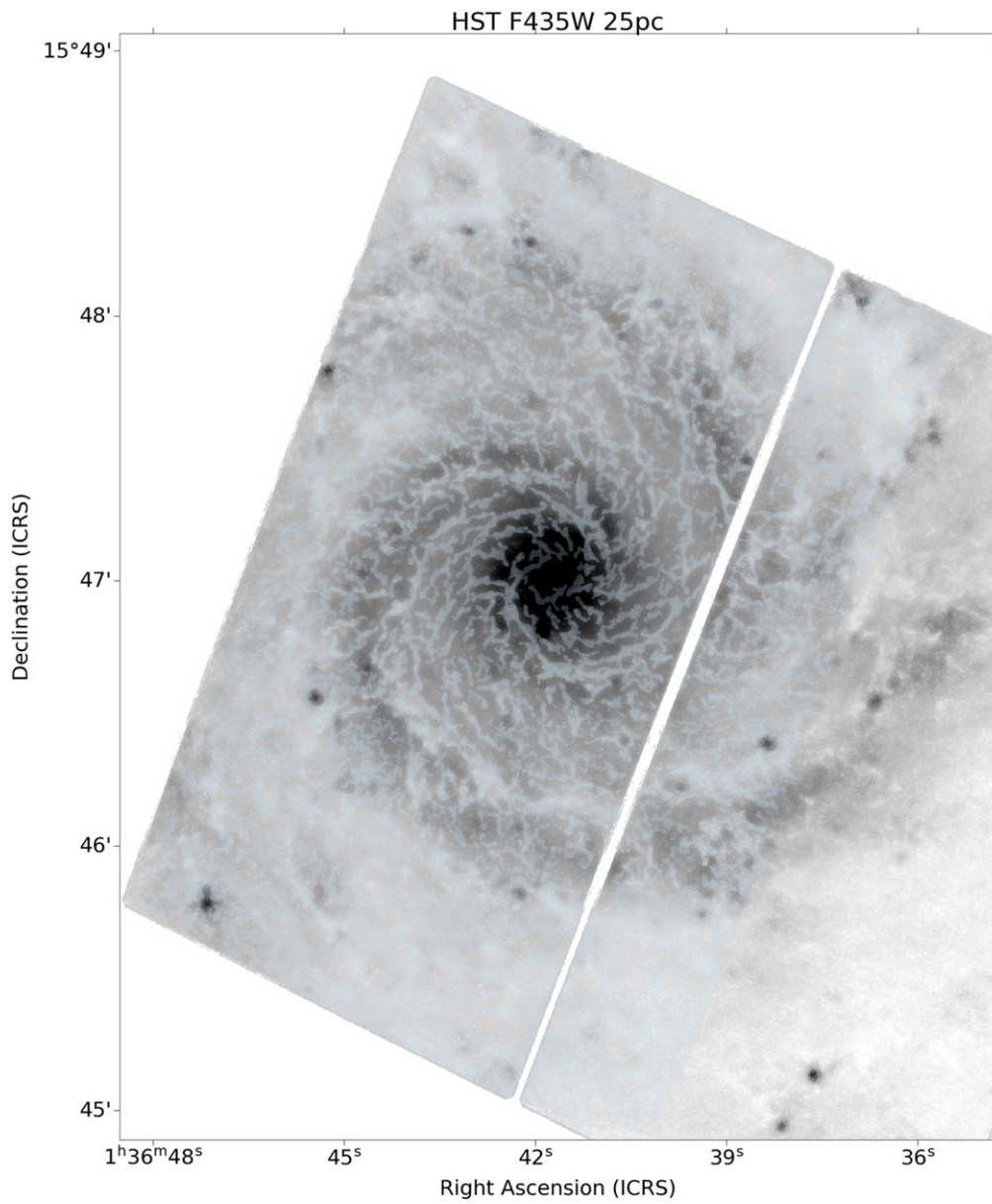


Figure A5. HST *B*-band (F435W) image with extracted attenuation filaments (25 pc scale) shown as transparent colored areas. The image is oriented north up and east left.

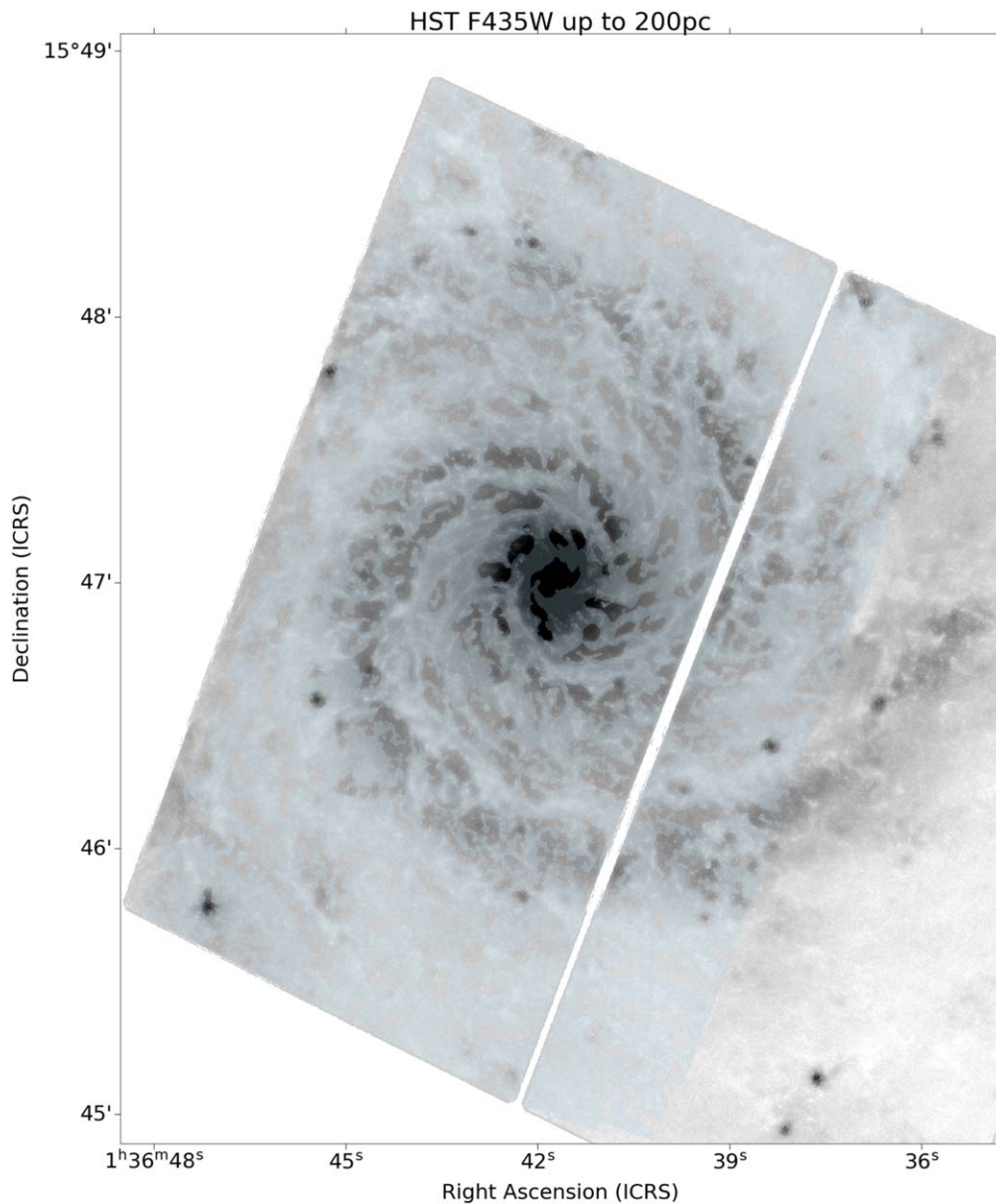













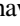












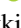



Figure A6. HST *B* band (F435W) image with extracted attenuation filaments (cumulative up to 200 pc scale) shown as transparent colored areas. The image is oriented north up and east left.

ORCID iDs

David A. Thilker  <https://orcid.org/0000-0002-8528-7340>
 Janice C. Lee  <https://orcid.org/0000-0002-2278-9407>
 Sinan Deger  <https://orcid.org/0000-0003-1943-723X>
 Ashley T. Barnes  <https://orcid.org/0000-0003-0410-4504>
 Frank Bigiel  <https://orcid.org/0000-0003-0166-9745>
 Médéric Boquien  <https://orcid.org/0000-0003-0946-6176>
 Yixian Cao  <https://orcid.org/0000-0001-5301-1326>
 Mélanie Chevance  <https://orcid.org/0000-0002-5635-5180>
 Daniel A. Dale  <https://orcid.org/0000-0002-5782-9093>
 Oleg V. Egorov  <https://orcid.org/0000-0002-4755-118X>
 Simon C. O. Glover  <https://orcid.org/0000-0001-6708-1317>
 Kathryn Grasha  <https://orcid.org/0000-0002-3247-5321>
 Jonathan D. Henshaw  <https://orcid.org/0000-0001-9656-7682>
 Ralf S. Klessen  <https://orcid.org/0000-0002-0560-3172>
 Eric Koch  <https://orcid.org/0000-0001-9605-780X>

J. M. Diederik Kruijssen  <https://orcid.org/0000-0002-8804-0212>
 Adam K. Leroy  <https://orcid.org/0000-0002-2545-1700>
 Ryan A. Lessing  <https://orcid.org/0000-0002-4089-1704>
 Sharon E. Meidt  <https://orcid.org/0000-0002-6118-4048>
 Francesca Pinna  <https://orcid.org/0000-0001-5965-3530>
 Miguel Querejeta  <https://orcid.org/0000-0002-0472-1011>
 Erik Rosolowsky  <https://orcid.org/0000-0002-5204-2259>
 Karin M. Sandstrom  <https://orcid.org/0000-0002-4378-8534>
 Eva Schinnerer  <https://orcid.org/0000-0002-3933-7677>
 Rowan J. Smith  <https://orcid.org/0000-0002-0820-1814>
 Elizabeth J. Watkins  <https://orcid.org/0000-0002-7365-5791>
 Thomas G. Williams  <https://orcid.org/0000-0002-0012-2142>
 Gagandeep S. Anand  <https://orcid.org/0000-0002-5259-2314>

Francesco Belfiore <https://orcid.org/0000-0002-2545-5752>
 Guillermo A. Blanc <https://orcid.org/0000-0003-4218-3944>
 Rupali Chandar <https://orcid.org/0000-0003-0085-4623>
 Enrico Congiu <https://orcid.org/0000-0002-8549-4083>
 Eric Emsellem <https://orcid.org/0000-0002-6155-7166>
 Brent Groves <https://orcid.org/0000-0002-9768-0246>
 Kathryn Kreckel <https://orcid.org/0000-0001-6551-3091>
 Kirsten L. Larson <https://orcid.org/0000-0003-3917-6460>
 Daizhong Liu <https://orcid.org/0000-0001-9773-7479>
 Ismael Pessa <https://orcid.org/0000-0002-0873-5744>
 Bradley C. Whitmore <https://orcid.org/0000-0002-3784-7032>

References

- Alina, D., Shomanov, A., & Baimukhametova, S. 2022, arXiv:2205.00683
 Anand, G. S., Rizzi, L., Tully, R. B., et al. 2021a, *AJ*, **162**, 80
 Anand, G. S., Lee, J. C., Van Dyk, S. D., et al. 2021b, *MNRAS*, **501**, 3621
 André, P., Di Francesco, J., Ward-Thompson, D., et al. 2014, in *Protostars and Planets VI*, ed. H. Beuther et al. (Tucson, AZ: Univ. of Arizona Press), 27
 Andre, P., Men'shchikov, A., Bontemps, S., et al. 2010, *A&A*, **518**, L102
 Astropy Collaboration, Robitaille, T. P., Tollerud, E. J., et al. 2013, *A&A*, **558**, A33
 Astropy Collaboration, Price-Whelan, A. M., Sipocz, B. M., et al. 2018, *AJ*, **156**, 123
 Baldwin, J. A., Phillips, M. M., & Terlevich, R. 1981, *PASP*, **93**, 5
 Barmby, P., Ashby, M. L. N., Bianchi, L., et al. 2006, *ApJL*, **650**, L45
 Barnes, A., Watkins, E., Meidt, S., et al. 2023, *ApJL*, 944, L22
 Belfiore, F., Leroy, A. K., Sun, J., et al. 2022, arXiv:2211.08487
 Bialy, S., Zucker, C., Goodman, A., et al. 2021, *ApJL*, **919**, L5
 Boquien, M., Burgarella, D., Roehly, Y., et al. 2019, *A&A*, **622**, A103
 Boquien, M., Kennicutt, R., Calzetti, D., et al. 2016, *A&A*, **591**, A6
 Bradley, L., Sipőcz, B., Robitaille, T., et al. 2022, *astropy/photutils: v1.5.0*, Zenodo, doi:10.5281/zenodo.6825092
 Buta, R. J., Sheth, K., Athanassoula, E., et al. 2015, *ApJS*, **217**, 32
 Butler, M. J., & Tan, J. C. 2009, *ApJ*, **696**, 484
 Calzetti, D. 2013, in *Secular Evolution of Galaxies*, ed. J. Falcón-Barroso & J. H. Knapen (Cambridge: Cambridge Univ. Press), 419
 Calzetti, D., Lee, J. C., Sabbi, E., et al. 2015, *AJ*, **149**, 51
 Carrière, J. S., Montier, L., Ferrière, K., & Ristorcelli, I. 2022, *A&A*, **668**, A41
 Chastenot, J., Sutter, J., Sandstrom, K. M., et al. 2023a, *ApJL*, 944, L22
 Chastenot, J., Sutter, J., Sandstrom, K. M., et al. 2023b, *ApJL*, 944, L11
 Crocker, A. F., Calzetti, D., Thilker, D. A., et al. 2013, *ApJ*, **762**, 79
 Dale, D. A., Boquien, M., Barnes, A., et al. 2023, *ApJL*, 944, L23
 Dharmawardena, T. E., Bailer-Jones, C. A. L., Fouesneau, M., & Foreman-Mackey, D. 2022, *A&A*, **658**, A166
 Dharmawardena, T. E., Bailer-Jones, C. A. L., Fouesneau, M., et al. 2023, *MNRAS*, **519**, 228
 Dong, H., Li, Z., Wang, Q. D., et al. 2016, *MNRAS*, **459**, 2262
 Duarte-Cabral, A., Acreman, D. M., Dobbs, C. L., et al. 2015, *MNRAS*, **447**, 2144
 Duarte-Cabral, A., & Dobbs, C. L. 2017, *MNRAS*, **470**, 4261
 Egorov, O., Kreckel, K., Sandstrom, K. M., et al. 2023, *ApJL*, 944, L16
 Emsellem, E., Schinnerer, E., Santoro, F., et al. 2022, *A&A*, **659**, A191
 Goodman, A. A., Alves, J., Beaumont, C. N., et al. 2014, *ApJ*, **797**, 53
 Green, C.-E., Cunningham, M. R., Dawson, J. R., et al. 2017, *ApJL*, **840**, L17
 Green, G. M., Schlafly, E., Zucker, C., Speagle, J. S., & Finkbeiner, D. 2019, *ApJ*, **887**, 93
 Groves, B., Kreckel, K., Santoro, F., et al. 2023, *MNRAS*, *Advance Access*
 Hacar, A., Clark, S., Heitsch, F., et al. 2022, arXiv:2203.09562
 Harris, C. R., Millman, K. J., van der Walt, S. J., et al. 2020, *Natur*, **585**, 357
 Hassani, H., Rosolowsky, E. W., Leroy, A. K., et al. 2023, *ApJL*, 944, L21
 Hinz, J. L., Rieke, G. H., Gordon, K. D., et al. 2004, *ApJS*, **154**, 259
 Hottier, C., Babusiaux, C., & Arenou, F. 2021, *A&A*, **655**, A68
 Hoversten, E. A., Gronwall, C., Vanden Berk, D. E., et al. 2011, *AJ*, **141**, 205
 Hunter, J. D. 2007, *CSE*, **9**, 90
 Jackson, J. M., Finn, S. C., Chambers, E. T., Rathborne, J. M., & Simon, R. 2010, *ApJL*, **719**, L185
 Jeffreson, S. M. R., Kruijssen, J. M. D., Keller, B. W., Chevance, M., & Glover, S. C. O. 2020, *MNRAS*, **498**, 385
 Koch, E. W., & Rosolowsky, E. W. 2015, *MNRAS*, **452**, 3435
 Kumari, N., Irwin, M. J., & James, B. L. 2020, *A&A*, **634**, A24
 La Vigne, M. A., Vogel, S. N., & Ostriker, E. C. 2006, *ApJ*, **650**, 818
 Lallement, R., Babusiaux, C., Vergely, J. L., et al. 2019, *A&A*, **625**, A135
 Lang, P., Meidt, S. E., Rosolowsky, E., et al. 2020, *ApJ*, **897**, 122
 Larson, K., Lee, J. C., Thilker, D. A., et al. 2022, *MNRAS*, submitted
 Lee, J. C., Sandstrom, K. M., Leroy, A. K., et al. 2023, *ApJL*, 944, L27
 Lee, J. C., Whitmore, B. C., Thilker, D. A., et al. 2022, *ApJS*, **258**, 10
 Leike, R. H., & Enßlin, T. A. 2019, *A&A*, **631**, A32
 Leike, R. H., Glatzle, M., & Enßlin, T. A. 2020, *A&A*, **639**, A138
 Leroy, A. K., Bigiel, F., de Blok, W. J. G., et al. 2012, *AJ*, **144**, 3
 Leroy, A. K., Hughes, A., Liu, D., et al. 2021, *ApJS*, **255**, 19
 Leroy, A. K., Sandstrom, K. M., Rosolowsky, E. W., et al. 2023, *ApJL*, 944, L9
 Liu, G., Koda, J., Calzetti, D., Fukuhara, M., & Momose, R. 2011, *ApJ*, **735**, 63
 Lonsdale Persson, C. J., & Helou, G. 1987, *ApJ*, **314**, 513
 Meidt, S. E., Rosolowsky, E. W., Jiayi, S., et al. 2023, *ApJL*, 944, L18
 Men'shchikov, A. 2021a, *A&A*, **654**, A78
 Men'shchikov, A. 2021b, *A&A*, **649**, A89
 Pineda, J. E., Arzoumanian, D., André, P., et al. 2022, arXiv:2205.03935
 Ragan, S. E., Henning, T., Tackenberg, J., et al. 2014, *A&A*, **568**, A73
 Rodriguez, J., Lee, J. C., Bradley, C., et al. 2023, *ApJL*, 944, L26
 Sale, S. E., & Magorrian, J. 2018, *MNRAS*, **481**, 494
 Sandstrom, K. M., Chastenot, J., Sutter, J., et al. 2023a, *ApJL*, 944, L7
 Sandstrom, K. M., Koch, E. W., Leroy, A. K., et al. 2023b, *ApJL*, 944, L8
 Santoro, F., Kreckel, K., Belfiore, F., et al. 2022, *A&A*, **658**, A188
 Smith, R. J., Glover, S. C. O., Clark, P. C., Klessen, R. S., & Springel, V. 2014a, *MNRAS*, **441**, 1628
 Smith, R. J., Glover, S. C. O., & Klessen, R. S. 2014b, *MNRAS*, **445**, 2900
 Smith, R. J., Glover, S. C. O., Klessen, R. S., & Fuller, G. A. 2016, *MNRAS*, **455**, 3640
 Smith, R. J., Treß, R. G., Sormani, M. C., et al. 2020, *MNRAS*, **492**, 1594
 Soler, J. D., Beuther, H., Syed, J., et al. 2020, *A&A*, **642**, A163
 Soubie, T. 2011, *MNRAS*, **414**, 350
 Sun, J., Leroy, A. K., Rosolowsky, E., et al. 2022, *AJ*, **164**, 43
 Syed, J., Soler, J. D., Beuther, H., et al. 2022, *A&A*, **657**, A1
 Thilker, D. A., Whitmore, B. C., Lee, J. C., et al. 2022, *MNRAS*, **509**, 4094
 Tress, R. G., Sormani, M. C., Glover, S. C. O., et al. 2020, *MNRAS*, **499**, 4455
 Treß, R. G., Sormani, M. C., Smith, R. J., et al. 2021, *MNRAS*, **505**, 5438
 Turner, J. A., Dale, D. A., Lee, J. C., et al. 2021, *MNRAS*, **502**, 1366
 Verley, S., Corbelli, E., Giovanardi, C., & Hunt, L. K. 2009, *A&A*, **493**, 453
 Verley, S., Hunt, L. K., Corbelli, E., & Giovanardi, C. 2007, *A&A*, **476**, 1161
 Viaene, S., Sarzi, M., Baes, M., Fritz, J., & Puerari, I. 2017, *MNRAS*, **472**, 1286
 Watkins, E. J., Barnes, A., Henny, K. F., et al. 2023, *ApJL*, 944, L24
 Zucker, C., Battersby, C., & Goodman, A. 2015, *ApJ*, **815**, 23
 Zucker, C., Battersby, C., & Goodman, A. 2018, *ApJ*, **864**, 153
 Zucker, C., Goodman, A., Alves, J., et al. 2021, *ApJ*, **919**, 35